Numerical study of continental collision: influence of buoyancy forces and an initial stiff inclusion

J. P. Vilotte *Centre Géologique et Géophysique, USTL, 34060 Montpellier, Cedex, France and Civil Engineering Department, University College Swansea, Swansea SA2 8PP*

R. Madariaga *Laboratoire de Sismologie, Institut de Physique du Globe, 4, Place Jussieu, 75230 Paris, Cedex 05, France*

M. Daignières *Centre Géologique et Géophysique, USTL, 34060 Montpellier, Cedex, France*

O. Zienkiewicz *Civil Engineering Department, University College Swansea, Swansea SA2 8PP*

Summary. We study simple models of collision between two continental plates patterned after the geometry of the India–Asia collision, but which may be applicable to more general situations. The collision is modelled by the indentation of a viscoplastic plate (Asia) by a rigid punch (India).

Although deformation is three-dimensional in nature, a plate thickness of the order of 100 km permits a 2-D approach for wavelengths longer than a few hundred kilometres. We assume an Airy compensation at the crust–mantle boundary throughout the deformation. We can then reduce the problem to a 2-D one within the context of thin plate theory. This model makes it possible to study crustal thickening during collisions.

The opposition between buoyancy forces, which tend to flatten the topography, and viscous resistance, appears clearly and we show the existence of a relaxation mechanism associated with the volumetric part of the deformation. The asymptotic behaviour of the model is of the incompressible plane strain type and thus crustal thickening tends to a maximum value. When this limit is reached no more thickening is possible and distensive phenomena can be induced. Buoyancy effects can be described by a non-dimensional parameter, the Argand number Ar, which is the ratio between the relaxation time and the characteristic time of the viscous flow.

A finite element approximation, based on a material description of the finite deformation, is used to investigate the evolution of the indentation process. The role of pre-existing heterogeneity (stiff inclusion) is also considered. Lateral boundary conditions on the plate are chosen to approximate the boundary interactions that are believed to apply for the Asian plate, i.e.

fixed boundaries to the east and the north and free boundaries to the west and the south.

For an homogeneous lithosphere the main influence of the buoyancy forces is to flatten the topography and to amplify a strong rotational extrusion process. Local distension can be induced but never in front of the indenter. Crustal thickening remains slight and smooth.

The presence of lithospheric heterogeneity perturbs the deformation pattern. Strong shear zones appear along the edges of the inclusions and control an intense extrusion process. Important rotational effects are observed during the extrusion as attested by a rigid rotation of the inclusion itself. The inclusion appears as a depression bounded by two thickened zones: one in front of the punch where the thickening is of the order of 100 per cent and another one in the northern part with a thickening of the order of 40–50 per cent.

The importance of lithospheric heterogeneity is clear when we compare numerical results with available elevation data in Asia.

1 Introduction

The geodynamic importance of continental collision processes has been emphasized by numerous authors who linked the deformation of vast continental areas to interactions occurring at the plate boundaries. Many areas have been studied: Asia (Tapponnier & Molnar 1976), the Mediterranean (Tapponnier 1977) or ancient terrains, like the Precambrian evolution of the pan-African belt (Caby, Bertrand & Black 1980). Collision mechanisms are very complicated, resulting from a succession of obduction and subduction processes with the final stages of collision being attributed to the resistance of continental lithosphere to subduction. However, before this final stage, important intracontinental deformation takes place as in the case of the present-day examples of New Guinea and Sulawesi in Indonesia (Silver, McCaffrey & Smith 1983).
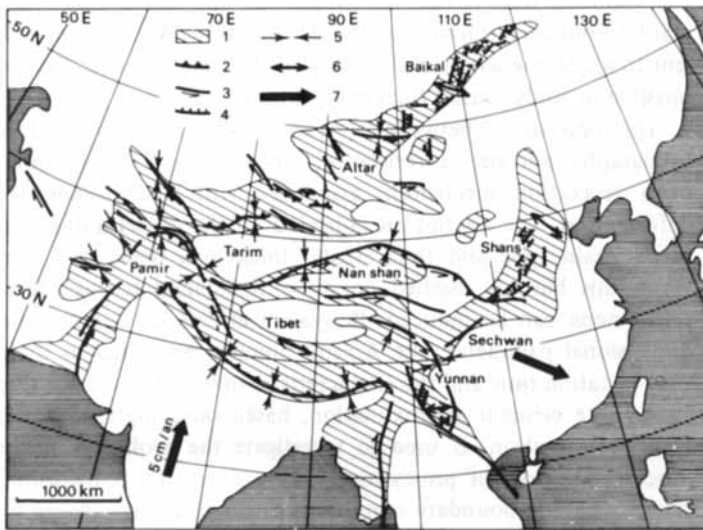

Figure 1. Outline structural geology map of Asia.

Schematically, continental collision usually occurs together with an important crustal thickening at the collision front (Tibetan plateau), and the development of long-scale positive gravimetric anomalies as in the Pan-African belt (Bayer & Lesquer 1980). Lateral extrusion of large continental masses towards adjoining zones has been proposed as a major consequence of this process by Tapponnier & Molnar (1976) and Tapponnier *et al.* (1983). The deformation associated with this extrusion process seems to be localized along major strike-slip fault zones, at least in the case of China.

One approach is to study the mechanical processes associated with continental collision as the deformation of a thin plate by a more rigid indenter, the rheology of the plate being that of a highly non-linear viscoplastic medium. Tapponnier & Molnar (1976) approached the problem by a simple analogy with plane strain deformation of a plate indented by a rigid punch. Such a model demonstrates many of the general kinematical properties of the deformation associated with collision but is limited only to the beginning stages of the collision and has all the drawbacks of slip-line theory on which the analysis is based. Another approach developed by Peltzer, Tapponnier & Cobbold (1982) and Tapponnier *et al.* (1983) is to study small-scale plasticine models which have the advantage, with respect to slip-line theory, of being able to model in an elegant way the finite deformation of the indented plate. A number of features observed in those experiments, particularly the development of large fractures, were related to large-scale faulting in Asia and the formation of marginal bassins by Tapponnier *et al.* (1983). Those experiments are, however, unable to model the effect of thickening and buoyancy forces in the crust. Numerical models seem to provide a natural way to extend the domain of investigation to more realistic although still schematic situations. Bird & Piper (1980) have presented numerical techniques for the generalization of the plane stress approximation to more realistic ones in strike-slip zones, and England & McKenzie (1982, 1983) have extended such an approach in order to allow the modelling of the initial stages of collision under special load conditions but rather restrictive boundary conditions. Vilotte, Daignieres & Madariaga (1982) modelled the plane stress and plane strain initial deformation of a plate under more general lateral boundary conditions, which are similar to those suggested by Tapponnier & Molnar (1976).

Numerical modelling appears particularly interesting because with a relatively modest computer expense many models with different rheologies and load conditions could be tested in order to study scaling effects. Further, such an approach may be used to analyse and scale laboratory models to field conditions. The two approaches are necessary if the correct rheologies and fracture properties are to be included in the models. However numerical models are the only practical way to include realistic buoyancy effects.

The present paper is a natural continuation of the modelling effort reported in Vilotte *et al.* (1984). However the modelling of buoyancy effects and of large finite deformation required some modifications in the numerical techniques. Although deformation processes occur necessarily in three dimensions and the role of vertical temperature profiles could be of major importance, the geometry of plates with thickness of the order of 100 km indicates that a 2-D approach should suffice for wavelengths longer than a few hundred kilometres. At these wavelengths, the topography is isostatically compensated and the assumption of Airy compensation at the crust—mantle boundary seems quite reasonable (England & McKenzie 1983). Using such a simple physical approach we reduce the problem to a 2-D one within the context of thin plate theory (Timoshenko & Woinowski-Krieger 1970). The opposite roles of the buoyancy forces (which tend to flatten the topography) and of viscous resistance (which opposes the flattening) appear quite clearly in our mechanical formulation. Topography relaxes with a time-scale of the order of several tens of Myr, which explains that in a steady state the bulge in front of the indenter tends to a constant height.

With this technique a number of numerical experiments are reported. Those include models with different ratios of buoyancy forces (Argand number, England & McKenzie 1983), and the presence of rheological heterogeneities like that which appears to be situated under the Tarim depression in Asia. We demonstrated in Vilotte *et al.* (1984) that such inclusions play a fundamental role in localizing plastic flow and creating shear zones. We show here that they could also affect the shape of the topography in a definite way. Rigid inclusions do not thicken and could be a possible mechanism for the creation of deep depressions inside a thickening plate.

2 Mechanical formulation

The time evolution of the deformation of a lithospheric plate under the combined effect of lateral buoyancy forces the subject of study here. Assuming an olivine creep rheology we reduce the problem to the study of a 2-D visco-plastic plate in which buoyancy appears as a rheological property.

2.1 RHEOLOGY AND KINEMATICS

Following Goetze (1978) and Kirby (1983) we adopt a viscoplastic rheology to describe the high temperature creep of lithospheric materials. As permanent change of shape occurs during the collision, elastic effects are in general insignificant (Tapponnier 1977; Vilotte *et al.* 1982) as far as the deformation phenomena is concerned. Adopting (as in Vilotte *et al.* 1982, 1984) an isotropic material and a simple von Mises yield criterion, it is possible to relate the current real (Cauchy) deviatoric stress tensor to the velocity gradient (Mandel 1971), and to the conjugate strain rate tensor via an incompressible fluid-like description (Zienkiewicz, Jain & Onate 1978):

$$\nabla v = \dot{R} \, R^T + \frac{\gamma\sqrt{3}}{2\sqrt{J_2}} < (\sqrt{3} \, \sqrt{J_2} - \sigma_y)^n > s \tag{1}$$

where **R** is the finite rotation tensor

$$s = \Gamma : \dot{\epsilon}; \quad \Gamma_{ijkl} = \mu \, \delta_{ik} \, \delta_{jl} + \mu \, \delta_{jk} \, \delta_{il} \tag{2}$$

where the equivalent viscosity μ is given by:

$$\mu = \frac{\sigma_y + (I_2/\gamma\sqrt{3})^n}{I_2} . \tag{3}$$

In (1) $\langle \cdot \rangle$ is used as follows:

$\langle f \rangle = f$ if $f \geqslant 0$ and $\langle f \rangle = 0$ if $f < 0$.

J_2 and I_2 are the second invariants of the Cauchy deviatoric stress tensor and strain rate tensor, respectively, σ_y is the yield stress and γ a temperature dependant fluidity parameter.

2.2 MOMENTUM BALANCE EQUATIONS

We study a quasi-static evolution of the deformation adopting a material description and an updated Lagrangian formulation where the reference configuration is continuously updated in order to coincide with the actual one.

$\Omega(t)$ being the reference configuration of the lithosphere at time t, the equilibrium equation can be written:

$$\nabla \cdot \sigma(t) - \rho \, \mathbf{g} = \mathbf{0} \text{ in } \Omega(t) \tag{4}$$

$$\nabla \cdot \mathbf{v}(t) \qquad = 0 \text{ in } \Omega(t) \tag{5}$$

and

$$\sigma(t) \cdot \mathbf{n}(t) = \tau(t) \text{ on } \partial_1 \Omega(t) \tag{6}$$

$$\mathbf{v}(t) \qquad = \widetilde{\mathbf{u}}(t) \text{ on } \partial_2 \Omega(t) \tag{7}$$

with

$$\sigma(t = 0) = \mathbf{s}_0 \text{ and } \mathbf{v}(t = 0) = \mathbf{v}_0. \tag{8}$$

Together with the constitutive relations this forms a well posed although intractable problem and the lack of geophysical constraints could hardly justify such an effort. For this reason we will make several approximations.

2.3 THIN PLATE FORMULATION AND DEPTH AVERAGED EQUATIONS

The vertical dimensions of the problem (≈ 100 km) are much smaller than the horizontal ones (≈ 1000 km). A natural approach is then to approximate the lithosphere as a thin plate lying on a substratum of much smaller viscosity. In addition we suppose that the wavelength of the horizontal variations of the topography is much greater than the thickness of the lithosphere. These hypotheses lead to the classical thin plate approximation

$$\sigma_{iz} \ll \sigma_{xx}, \sigma_{yy}, \sigma_{xy}, \sigma_{zz} \quad i = x, y. \tag{9}$$

Such an approximation is certainly not valid for the mountain ranges themselves where plate flexure and important crustal gradient play an important role, but should be valid for modelling the deformation of the continental domain behind the collision boundary.

Furthermore we assume that the horizontal velocity field is also independent of depth. This condition may be relaxed but would lead to unnecessarily complicated models (Zienkiewicz & Heinrich 1979). The deviatoric stress field s still depends on z through the
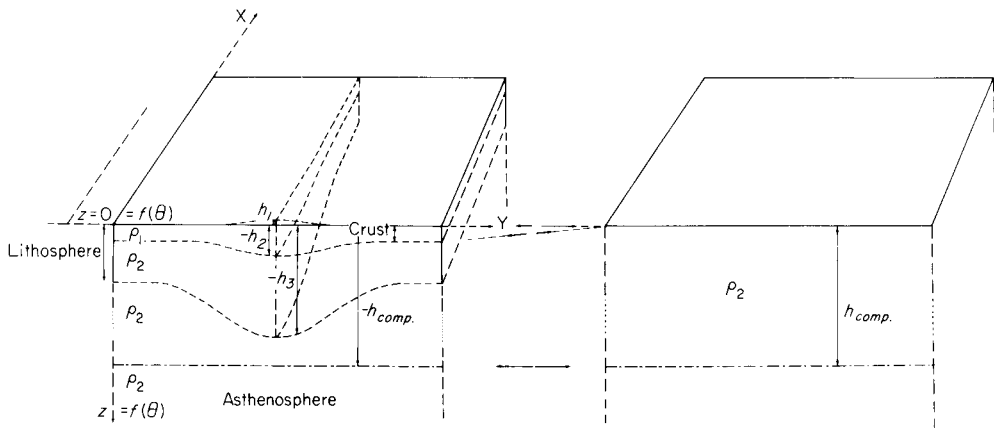

Figure 2. Reference hypothetical earth model for Airy's compensation.

depth dependence of the equivalent viscosity which is in turn controlled by the temperature dependence of the fluidity parameters.

In order to reduce the problem to a 2-D one we average over depth. Integrating the incompressibility equation (5) and assuming that the crust and mantle are chemically differentiated, we get:

$$\partial_i(h_\beta \, v_i) = -h_\beta \quad i = x, y \tag{10}$$

where β stands for (c) crust, (m) mantle, or (l) lithosphere. Therefore any increase in crustal thickness has to be matched by a lithospheric mantle thickening so that:

$$h_c/h_m = \alpha \quad \text{and} \quad h_c/h_l = \alpha/(1 + \alpha). \tag{11}$$

In order to integrate the equilibrium equation (4) we introduce (Fig. 2) a coordinate system centred at the surface of a hypothetical earth model without crust. Then the top and bottom of the crust are at h_1 and $-h_2$ respectively, the bottom of the mechanically competent lithosphere at a depth $-h_3$. The averaged equilibrium equation can then be written as:

$$\partial_j(h_1 \, \sigma_{ij}) + p_3 \, h_{3,i} = 0 \tag{12}$$

where σ is the vertically averaged Cauchy stress tensor and $p_3 = p(h_3)$.

2.4 ISOSTASY HYPOTHESIS

In the lithosphere the density heterogeneities are gravitationally compensated, for wavelengths longer than a few hundred kilometres. We assume that in the course of the continental collision the crustal thickness is continuously compensated according to Airy's mechanism. Assuming a constant density for the crust and mantle we find now for the averaged equilibrium:

$$\partial_j(h_1 \, \sigma_{ij}^e) = 0 \quad i, j = x, y \tag{13}$$

where σ^e is the effective mean stress:

$$\sigma_{ij}^e = -p^e \, \delta_{ij} + 2\mu \, \dot{\epsilon}_{ij} \tag{14}$$

with

$$p^e = \frac{1}{h_1} \left[\rho_1 \, (1 - \rho_1/\rho_2) \, g \, h_c^2 + \rho_2 \, g \, \frac{h_3^2}{2} \right] - \mu(\dot{\epsilon}_{xx} + \dot{\epsilon}_{yy}). \tag{15}$$

Note that buoyancy forces enter now into equilibrium equations through the vertically averaged lithospheric pressure (the first term on the right in (15) depends on the history of the vertical deformation while the second is an instantaneous viscous resistance).

Airy's hypothesis adopted here implies that isostatic equilibrium is verified at every time on the course of viscoplastic deformation of the lithosphere. This approximation may only apply if the deformation necessary to ensure isostasy occurs with a time-scale which is shorter than that associated with large-scale horizontal deformation due to collisions. This is approximately verified for long wavelengths. For a short time-scale and near the collision front the elastic deformation of the plates may be important as shown by Lyon Caen & Molnar (1983) and Karner & Watts (1983).

The vertically averaged viscosity entering into (14) has been defined in Vilotte *et al.* (1982, 1984) and is in fact controlled by the most competent part of the lithosphere as defined by Kirby (1983). Note that assuming that the thermal relaxation time is long with

respect to that of the horizontal flow of the lithosphere, the isotherms follow the deformation of the material. In this case the averaged viscosity becomes independent of the vertical deformation of the lithosphere for a linear temperature gradient.

3 Dimensional analysis

We introduce the following characteristic dimensions: L, the scale length of boundary forces (i.e. dimensions of punch); and U, the velocity at which the punch advances.

Such a choice implies a characteristic time for the flow:

$$t_c = L/U. \tag{16}$$

A straightforward analysis allows us to rewrite the equilibrium equation (13) as:

$$-A_R \, h_c^* \, \nabla^* h_c^* + \nabla^* [h_1^* \mu^* \, (\nabla^* . \, \mathbf{V}^*)] + \nabla^* . \, [h_1^* \mu (\nabla^* \, \mathbf{v}^* + \mathbf{v}^* \nabla^*)] = 0 \tag{17}$$

where * denotes a dimensional variable and:

$$A_R = \frac{\rho_1(1 - \rho_1/\rho_2) \, g \, L}{(1/\bar{\gamma}\sqrt{3})^{1/n} \, (U/L)^{1/n}} = \frac{t_c}{\tau_m} \tag{18}$$

$$\bar{\mu}^* = [K \, I_2^{*-1} + I_2^{* \, (1/n-1)}] \tag{19}$$

with

$$K = \frac{\sigma_y}{(1/\bar{\gamma}\sqrt{3})^{1/n} \, (U/L)^{1/n}} \tag{20}$$

and $\bar{\gamma}$ is readily obtained from Vilotte *et al.* (1984). The number K was introduced in Vilotte *et al.* (1982, 1984) as the ratio between plastic yield stress and viscosity. Argand's number was introduced by England & McKenzie (1982).

τ_m is the relaxation time, corresponding to the topography relaxation mechanism and is the delay compared with a situation where no more local thickening is possible.

The Argand number can also be interpreted as a measure of the competition between two processes: relaxation in the vertical plane due to buoyancy forces which tends to produce a plane strain situation, and horizontal flow controlled by the geometry and the boundary conditions in the horizontal plane.

For a stiff lithosphere ($\tau_m \gg t$), the relaxation process would be slow compared to the flow time-scale and h becomes entirely controlled by the horizontal flow field, via its incompressibility property. The deformation tends to a plane stress regime.

For a soft lithosphere ($\tau_m \ll t$), the relaxation process would dominate and the lithosphere appears to be clamped by gravity. Plane strain conditions dominate and we are in the situation of Tapponnier & Molnár (1976) or in the experimental conditions of Peltzer, Tapponnier & Molnar (1982) where a plasticine plate is clamped between two rigid plates during the indentation process.

For a normal lithosphere: $\tau_m \approx t$ and the relaxation of the thickening process now plays a fundamental role during the deformation of the lithosphere.

4 A linearization study

Although the problem is well posed, its solution and its physical understanding are difficult due to the high non-linearities. It seems therefore that not only a careful numerical analysis

has to be performed but as usual a physical intuition of the role of the different parameters previously pointed out has to be improved through a linearized approach.

Let us choose a reference configuration for the lithosphere in which the crustal and lithospheric thickness satisfy:

$$\nabla \bar{h}_c = 0 \quad \text{and} \quad \nabla \bar{h}_1 = 0. \tag{21}$$

We only consider here small perturbations around that configuration:

$$h_c = \bar{h}_c + \delta h_c \quad \text{and} \quad h_1 = \bar{h}_1 + \delta h_1. \tag{22}$$

The lithosphere is also characterized by a linear averaged viscosity. It is then obvious that the isotropic part of the deformation presents a relaxation mechanism as expressed by:

$$\delta \bar{\sigma}^{Pe} = \frac{1}{2} \, (\bar{\sigma}^e : I)I = \frac{\alpha}{(1 + \alpha)} \, \rho_1 (1 - \rho_1/\rho_2) g \, \delta h_c + 3 \bar{\mu} \, h_c / \bar{h}_c. \tag{23}$$

Such a relation is of the Kelvin–Voight type. The mechanism of compensation is directly incorporated into the averaged constitutive equation which presents a pure viscous deviatoric part and a type of 'viscoelastic' isotropic one.

In order to clarify this relaxation mechanism, let us consider the simple case when $\delta \bar{\sigma}^{Pe}$ is a simple Heaviside function. We then get, by a Laplace transform analysis:

$$\delta h \, (t) = \delta \bar{\sigma}^{Pe} \, F_\alpha^{-1} \, [1 - \exp \, (-t/\tau'_m)] + h_0 \exp \, (-t/\tau'_m) \tag{24}$$

with

$$F_\alpha = \frac{\alpha}{1 + \alpha} \, \rho_1 g(1 - \rho_1/\rho_2) \quad \text{and} \quad \tau'_m = \bar{\mu}/F_\alpha \bar{h}_c \tag{25}$$

and so

$$\nabla . \mathbf{v}(t) = \frac{1}{\tau'_m} \, (1 + 1/F_\alpha \bar{h}_c) \exp(-t/\tau'_m). \tag{26}$$

Thus, when $t \rightarrow \infty$:

$$\delta h_c(t) \rightarrow \delta \bar{\sigma}^{Pe}/F_\alpha \tag{28}$$

while

$$\nabla . \mathbf{v}(t) \rightarrow 0.$$

The deformation tends asymptotically to a local incompressible plane strain regime (in two dimensions) and τ'_m measures the time necessary to reach this plane strain mode of deformation.

5 Numerical experiments

We consider a continental lithospheric section of finite dimension with initial geometry ABCD as shown in Fig. 3. The plate is punched at $t = 0$, by a rigid indenter of rectangular shape. The choice of boundary conditions is difficult since they have to replace the interaction between the studied plate and the neighbouring ones. In particular, the effect of the punch is regarded as a contact problem and is simply replaced by the application of a constant velocity U, on a section (MN) of the boundary AB. The boundary BC is free of deviatoric stress. The boundary DC is free-slide, limiting the extension of the deformation.
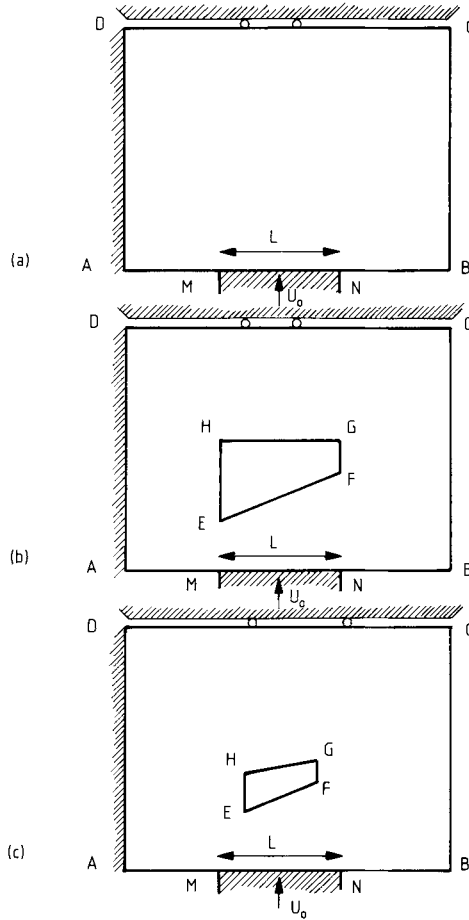
Figure 3. Geometry of the numerical models: (a) homogeneous plate, (b) heterogeneous plate: large stiff inclusion, (c) heterogeneous plate: small stiff inclusion.

Finally, boundary AD is considered as fixed (i.e. zero velocity). This choice of boundary conditions was discussed by Vilotte *et al.* (1982). A zero normal gradient condition has been imposed on the plate thickness on boundary MN for continuity requirements.

The present study has been done in a non-dimensional form, and the characteristic parameters are those previously defined: Ar, K, n.

However, in order to clarify the magnitude of the variables, reference values are listed in Table 1, following those previously used in Vilotte *et al.* (1984). The values of γ are very uncertain since a change on the lower and mainly upper isotherms (i.e. the definition of the strength layer) leads to important variations of γ. For this reason, we have systematically investigated for a fixed K, the influence of the Argand number on the deformation. Argand values of 300, 500, 700, 900 were studied while K was taken as 2.69 or 0 and $n = 3$.

In Section 5.2 inclusion of geometry EFGH is considered inside the plate (Fig. 3b, c). Such a heterogeneity is described in term of a rigidity ratio R as introduced in Vilotte *et al.* (1984):

$$R = \bar{\sigma}_y^{(2)}/\bar{\sigma}_y^{(1)} \quad \text{or} \quad [\bar{\gamma}^{(1)}/\bar{\gamma}^{(2)}]^{1/n} \tag{29}$$

Table 1. Typical parameter values for the model.

Geometrical parameters:	MN (L) = 2.4 Mm
	AD = 2.0 × MN
	NB = 1.2 × MN
Kinematical parameters:	$U = 1.6 \times 10^{-9}$ m s^{-1} (5 cm yr^{-1})
Rheological parameters:	$n = 3.0$
	$\bar{\sigma}_y = 30.0$ MPa (0.3 kb)
	$\bar{\gamma} = 2.7 \times 10^{-37}$ Pa^{-3} s^{-1}
Buoyancy parameters:	$\rho_1 = 2.7$ Mg m^{-3} (crustal density)
	$\rho_2 = 3.3$ Mg m^{-3} (mantle density)
	$h_c = 3 \times 10^4$ m (initial crustal thickness)
	$h_m = 10^4$ m (initial lithospheric thickness)

where indexes (1) and (2) stand for the material of the plate and the inclusion, respectively. The first expression is obtained for $\bar{\gamma}^{(1)} = \bar{\gamma}^{(2)}$ and the second for $\sigma_y^{(1)} = \sigma_y^{(2)}$ with n constant in both cases. Results are presented for a relatively small ratio $R \approx 2.5$ and for two sizes of the inclusion (Fig. 3b, c). A systematic study of the influence of the ratio R on the deformation evolution is reported elsewhere (Vilotte *et al.* 1984), for plane strain deformation.

The numerical formulation of the problem is reported in the Appendix. The problem is solved via a finite element method. The plate is divided into a coarse mesh of 88 isoparametric quadratic elements (9-noded rectangle of the Lagrange family). As mentioned before, the problem is formulated in an updated Lagrangian description: the reference configuration is continuously updated and is chosen in order to match at each time t the evolution of the actual configuration. The mesh is therefore updated at every time step after integrating the velocity field obtained at equilibrium. Such an integration can be performed explicitly or implicitly (Zienkiewicz 1984), both have been tested and used, the major drawback of the last one being the increase of CPU time.

This kind of approach allows us to follow the finite deformation and is suitable for geophysical problems where only the deformation in the deformed configuration is available. Any comparison with present data has to be performed on such a deformed configuration.

Results are presented as isovalue contour maps superimposed on the deformed geometry of the plate. The quantities are first determined at the nodal points of the mesh using a variational recovery technique. Then each element is divided into six or more linear triangles, and the physical variables are interpolated at the new nodes using quadratic shape functions. Inside each triangle, the interpolation is linear.

Successive cross-sections of the crustal thickness (here proportional to the topography) have been computed during the evolution of the deformation, along a constant profile as shown on Fig. 3 perpendicular to the punch.

5.1 HOMOGENEOUS LITHOSPHERE

A systematic investigation of the influence of the Argand number on the deformation was done, and only some of the most relevant results are presented here.

Results for Ar = 300 and 700 are shown in Figs 4–6, and 7–9 (A, B) for Ar = 500. Fig. 13 shows the influence of the Argand number on the evolution of the crustal thickness, along a cross-section running through the mesh, normal to the punch as discussed before and this for Ar = 300, 500, 700, 900 and different time of evolution: $t = 0.24\ t_c$ and 0.84 t_c, where $t_c = L/U \approx 47$ Myr.
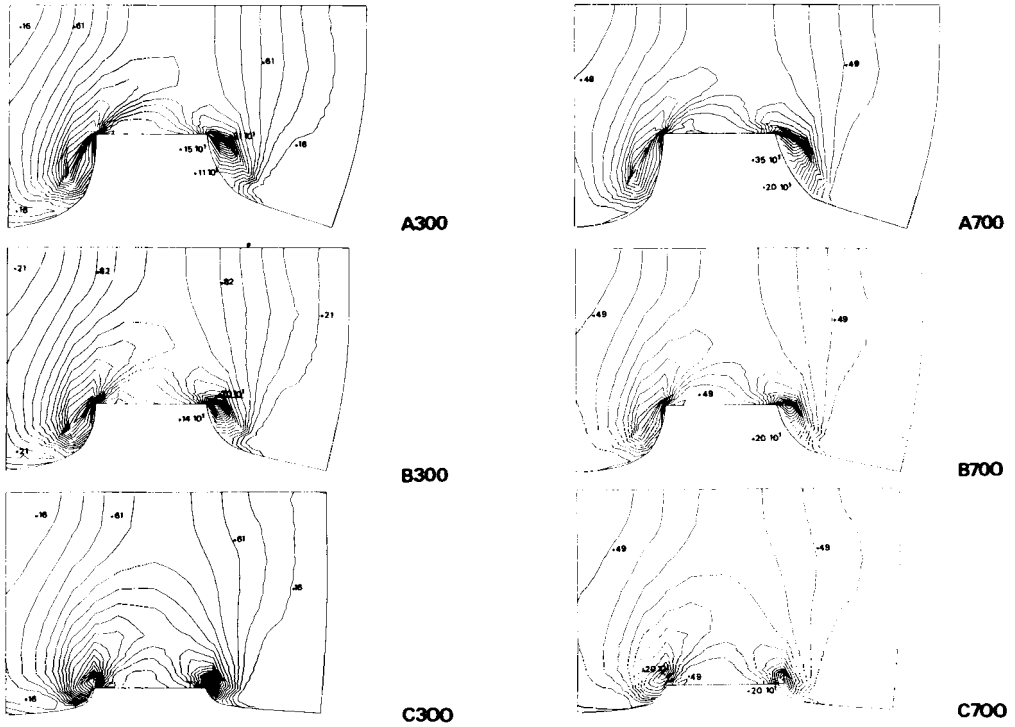
Figure 4. Second invariant of the strain rate tensor for homogeneous plate at A: $0.84 t_c$, B: $0.6 t_c$, C: $0.24 t_c$ ($t_c = L/U = 47$ Myr) and for Ar = 300 and 700 respectively in the left and right sides of the figure: A700: 20 isovalues (0.24, 4.9, step: 0.24), B700: 17 isovalues (0.24, 4.1, step: 0.24), C700: 14 isovalues (0.24, 3.4, step: 0.24), A300: 20 isovalues (0.15, 3.0, step: 0.15), B300: 19 isovalues (0.15, 2.8, step: 0.15), C300: 19 isovalues (0.15, 2.8, step: 0.15).

The influence of the yield stress was also studied and the results are presented for $K = 2.69$ and compared to the creep for Ar = 500 in Figs 7–9 and 14.

5.1.1 Second invariant of the strain rate tensor

The second invariant of the strain rate tensor, defined as:

$$I_2 = \dot{\epsilon} : \dot{\epsilon} = \dot{\epsilon}_{ij} \dot{\epsilon}_{ij}$$

depends now on the vertical strain rate, i.e. on the horizontal dilatation

$$\dot{\epsilon}_{zz} = -(\dot{\epsilon}_{zz} + \dot{\epsilon}_{yy}).$$

However, since $L \gg H$, the horizontal deformation dominates and will control the isovalue of I_2 and we will then find again some common features with plane strain results.

Maximum shear is localized on both sides of the punch (Fig. 4), in relation to its two geometrical singularities. These two shears present a non-symmetrical evolution. The main shear zone develops from the earliest stage of the evolution, on the east side of the punch near the fixed boundary AD. This shear is progressively stretched and bent during the punch penetration, in relation to a strong rotational effect controlled by the free boundaries MB and BC. The importance of such a rotational effect was discussed in the plane strain analysis of Vilotte *et al.* (1984). This shear bending effect in front of the punch contributes to a progressive localization of the main deformation in the vicinity of the indenter.
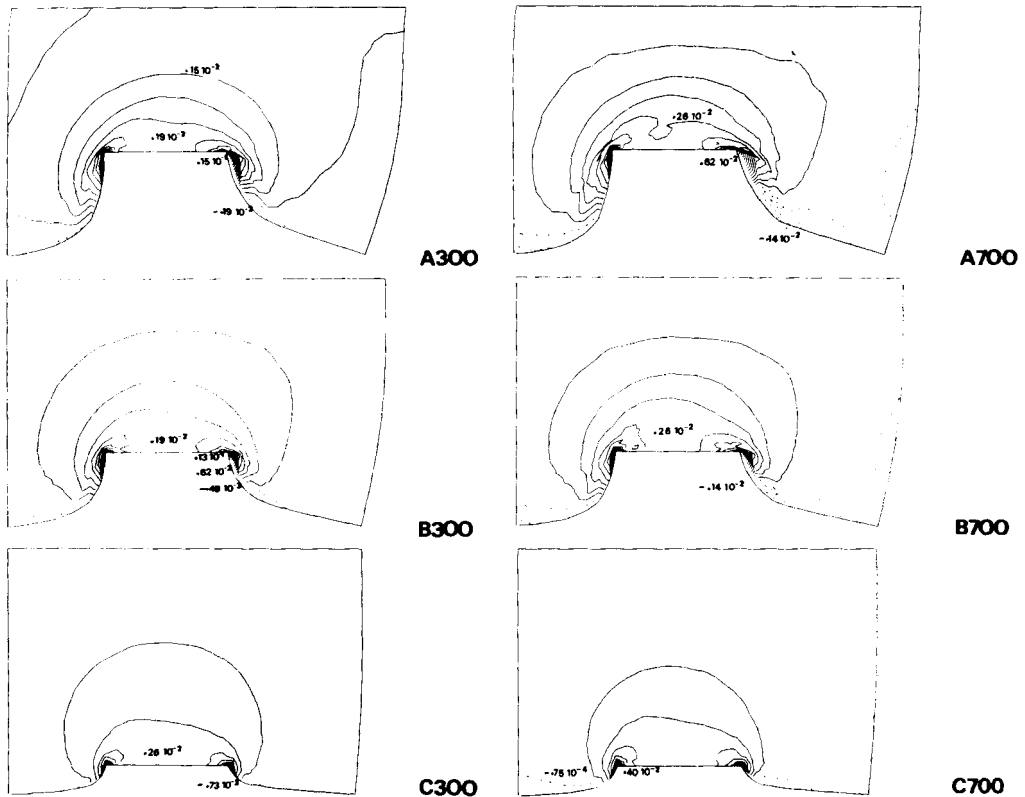
Figure 5. Normalized crustal thickness variation ($h - h_0/h_0$) for an homogeneous plate, same as Fig. 4: A700: 20 isovalues ($- 0.21 \times 10^{-2}$, 0.10×10^{-1}, step: 0.67×10^{-3}), B700: 18 isovalues ($- 0.14 \times 10^{-2}$, 0.10×10^{-1}, step: 0.67×10^{-3}), C700: 13 isovalues ($- 0.75 \times 10^{-3}$, 0.73×10^{-1}, step: 0.67×10^{-3}), A300: 19 isovalues ($- 0.18 \times 10^{-2}$, 0.18×10^{-1}, step: 0.11×10^{-3}), B300: 18 isovalues ($- 0.15 \times 10^{-2}$, 0.17×10^{-1}, step: 0.11×10^{-3}), C300: 11 isovalues (-0.73×10^{-3}, 0.10×10^{-1}, step: 0.11×10^{-3}).

Maximum shear is confined on the side of the punch and results from an ejection of material, initially located at the corner of the indenter, and which progressively moves towards the free boundaries adjoining the punch.

The boundary conditions play a very important role here. The fixed boundary AD induces a rotation allowing the material to escape through the free boundary AM, as this one is stretched by the penetration of the punch. This rotation interacts with the one controlled by the geometrical singularity of the indenter described earlier and extends more outside the deformation. The free boundary BC, on the other hand, allows and controls an important E—W flow with strong rotational effects near the corner of the punch. Such a rotational flow explains the geometry and the bending of the boundary BC, in particular near the corner B.

The bending of the shear in front of the punch is not only controlled by the free boundary BC but also by the distance between the contact boundary MN and the free-glide one at DC. If this boundary is moved away from the punch, i.e. at a distance of 2.5 or 3.0 MN, the shear zones do not present such a bending effect and become sub-parallel to the direction of indentation, the indenter working then more or less as a snow-plough. On the contrary, if the free-glide boundary is brought closer to MN, bending increases, producing a strong lateral extrusion process as will be noticed in the heterogeneous lithosphere example.
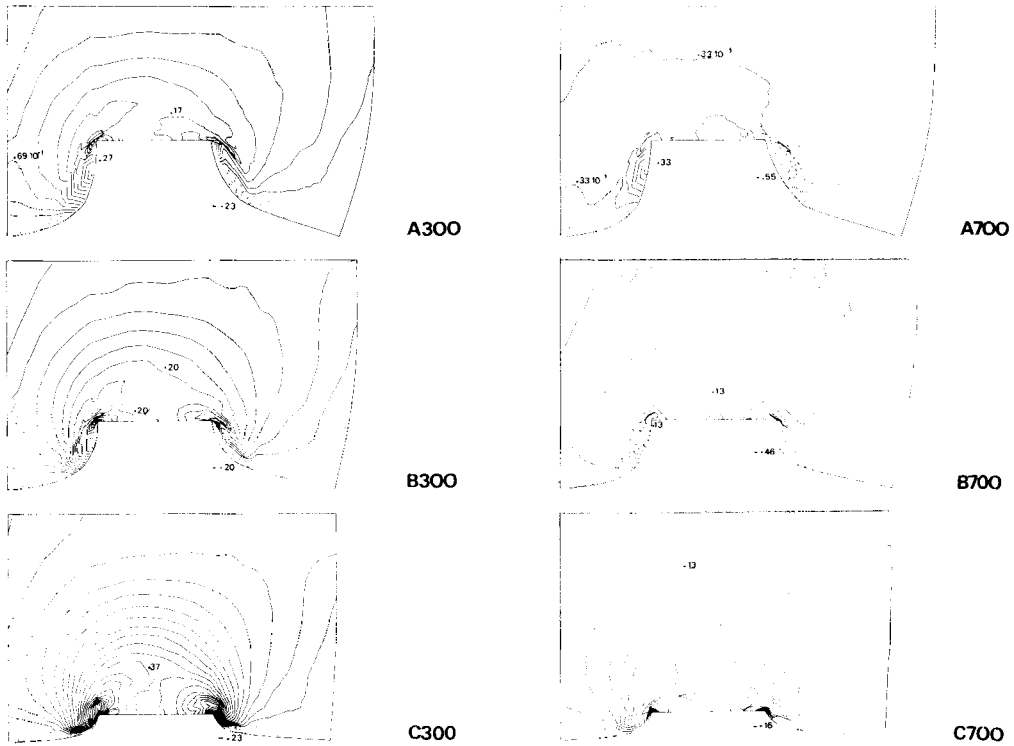
Figure 6. Vertical strain rate for homogeneous plate, same as Fig. 4: A700: 19 isovalues (– 0.60, 0.27, 0.49 × 10⁻¹), B700: 16 isovalues (– 0.45, 0.27, 0.49 × 10⁻¹), C700: 18 isovalues (– 0.21, 0.62, 0.49 × 10⁻¹), A300: 19 isovalues (– 0.22, 0.36, 0.33 × 10⁻¹), B700: 22 isovalues (– 0.22, 0.46, 0.33 × 10⁻¹), C700: 46 isovalues (– 0.22, 1.26, 0.33 × 10⁻¹).

The propagation of these shear zones is brought about by the advance of the punch rather than resulting from a physical process, such as the propagation of an instability. This lack of physical instabilities is characteristic of the indentation process.

Influence of the Argand number. The principal effect of the Argand number is to localize the shear in the vicinity of the indenter.

As the Argand number increases, the shear zones show a smaller extension in front of the punch, and during the indentation process a rigid zone develops near the free boundary BC.

Anticipating the discussion on the crustal thickness evolution, one can show that this localization is related to the flattening, as Ar increases, of the strong topography localized in the vicinity of corners of the punch which in turn implies an horizontal redistribution of that material. This phenomenon explains the evolution of the shear zone associated with the boundary NB. The intensity of the lateral shears increases with Ar while their geometry does not significantly change.

Influence of the plastic effects ($K = 2.69$). The main effect of plasticity is a strong localization of the deformation. This localization is due to the increase of the rheological non-linearity of the plate. As previously mentioned in Vilotte *et al.* (1982), an increase of σ_y or n leads to very similar effects in terms of the deformation geometry, and indeed in both cases K is increased.
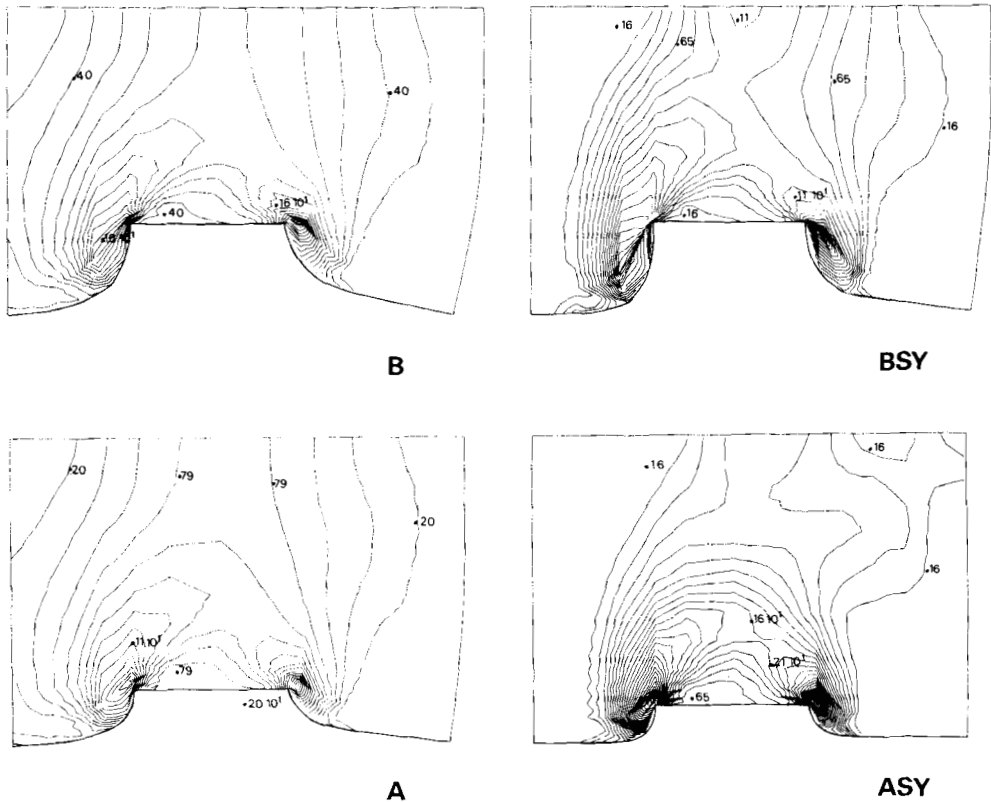
Figure 7. Second invariant of the strain rate tensor for homogeneous plate at Ar = 500: for power law creep ($n = 3$, $K = 0$) A = 0.24 t_c, B = 0.6 t_c; for plastic flow ($n = 3$, $K = 2.69$) ASY = 0.24 t_c, BSY = 0.6 t_c; A: 16 isovalues (0.19, 3.15, 0.19), B: 17 isovalues (0.19, 3.35, 0.19), ASY: 27 isovalues (0.16, 4.38, 0.16), BSY: 20 isovalues (0.16, 3.24, 0.16).

Shear intensity and deformation gradients are increased with K, because of very strong and localized rotational effects. Rigid zones expand and the deformed zone is confined between two essentially rigid walls.

5.1.2 Crustal thickening

Crustal thickness shows a non-symmetrical geometry, due to the boundary conditions.

Crustal thickness spreads towards and is contained by the fixed boundary AD, while at the free boundary BC a flow is induced which extrudes the material in front of the punch laterally.

The geometrical singularities of the punch absorb most of the crustal thickening, and apart from these very localized areas the thickening of the crust remains relatively small (Fig. 13) whatever the Argand number is.

The rotation-driving mechanism leads to a progressive localization of the thickening in the areas adjoining the punch (Fig. 5). These areas are located in the same place as those of strong pressure (Vilotte *et al.* 1984), and of strong shear (Nguyen 1981) in plane strain analysis.

The crustal thickness shows a smooth topography (Fig. 13) and decreases gently towards
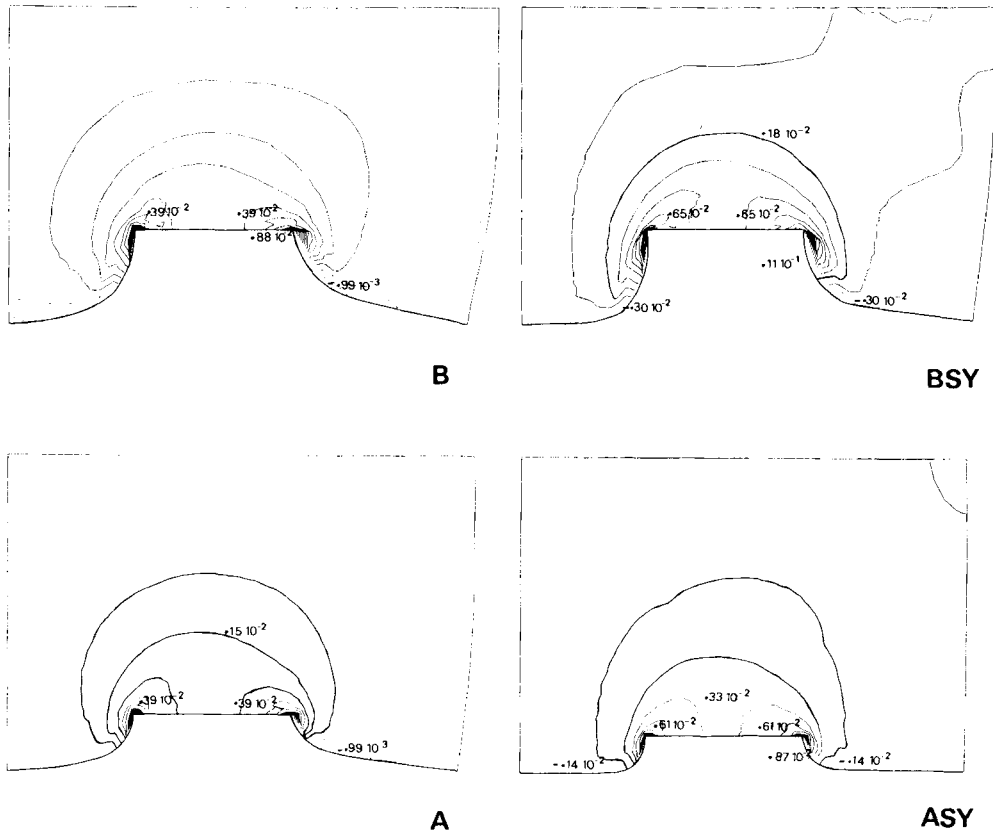
Figure 8. Normalized crustal thickness variation $(h - h/h)$ for homogeneous plate at Ar = 500, same as Fig. 7: A: 15 isovalues $(- 0.99 \times 10^{-2}, 0.10 \times 10^{-1}, 0.81 \times 10^{-3})$, B: 19 isovalues $(- 0.18 \times 10^{-2}, 0.13 \times 10^{-1}, 0.81 \times 10^{-3})$, ASY: 14 isovalues $(- 0.14 \times 10^{-2}, 0.17 \times 10^{-1}, 0.15 \times 10^{-3})$, BSY: 19 isovalues $(- 0.30 \times 10^{-2}, 0.25 \times 10^{-1}, 0.15 \times 10^{-3})$.

the free-glide boundary DC. Thinning processes do not occur in front of the punch (Fig. 5), but take place laterally to the punch in the vicinity of the free boundaries. They are confined and of small intensity. The location of these thinning zones is related to the warping of the plate in response to the rotational part of the finite transformation, in particular on the east side of the plate.

Influence of the Argand number. As the Argand number increases, crustal thickening tends to spread over the plate. This spreading is related to the flattening effect of the Argand number, which imply a flow redistribution of the material toward the horizontal plane and a stronger coupling between horizontal flow and vertical deformation (Fig. 13). The thickening of the crust never exceeds 20—40 per cent whatever the Argand number is, which is small, and no plateau geometry is observed in front of the punch. The influence of the Argand number on the thinning process remains small, due to the smaller order of magnitude of such phenomena.

Influence of the plastic effects. The non-linearity effects tend once more to localize the phenomena in the vicinity of the indenter and especially near its corners (Fig. 8).
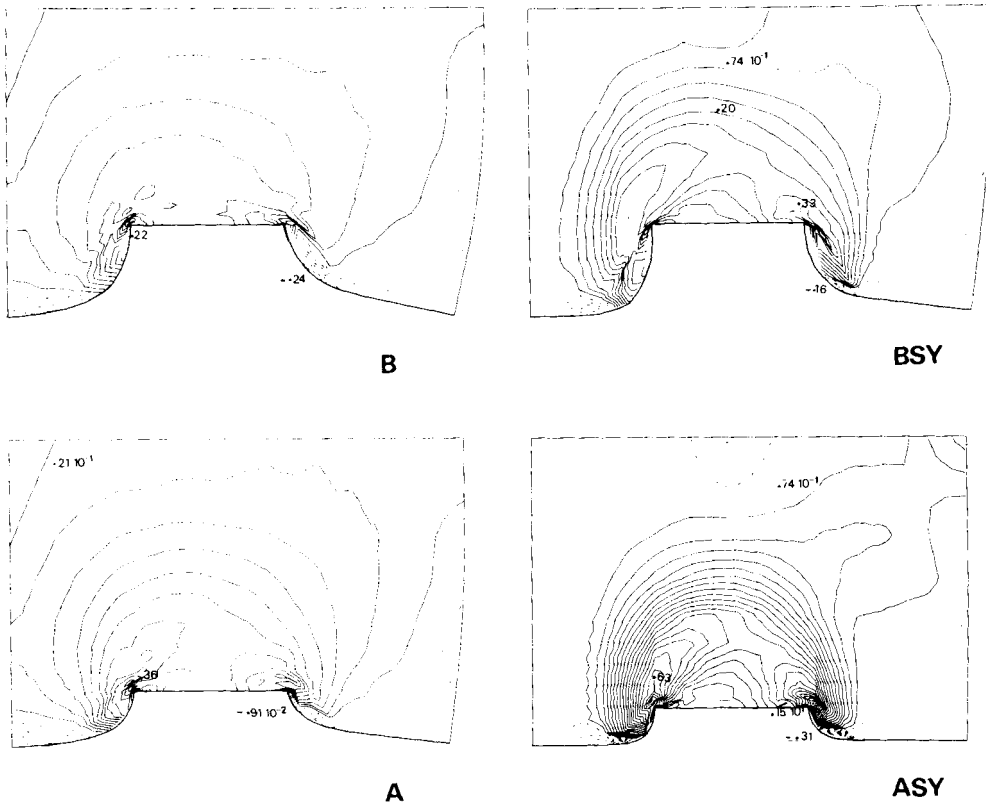
Figure 9. Vertical strain rate for homogeneous plate at $Ar = 5000$, same as Fig. 7: A: 21 isovalues (-0.20, 0.54, 0.37×10^{-1}), B: 19 isovalues (-0.27, 0.31, 0.37×10^{-1}), ASY: 48 isovalues (-0.55, 1.42, 0.42×10^{-1}), BSY: 25 isovalues (-0.22, 0.79, 0.42×10^{-1}).

In front of the indenter (Fig. 14), the crustal thickening is now more noticeable and could reach 40–70 per cent. It decreases abruptly showing a plateau-forming effect. This sharp decrease to the north of the crustal thickening can lead near the free-glide boundary DC to some local thinning process. The Argand number plays an increasing role as the rheological non-linearity and then the thickening gradients come to be important.

The thinning zones (Fig. 8) seem to be even more restricted to the neighbouring free boundaries and of small importance.

5.1.3 Vertical strain rate

Vertical strain rates are instantaneous measures of the vertical deformation. Because of the integrated nature of the crustal thickness, and the advective transport associated with finite transformation, the vertical strain rate field geometry does not match the crustal thickness one and indeed provides further physical information.

Thickening evolution tends progressively to a limit, as it is attested by the decrease of the vertical strain rates, which can even lead to a limited distensive area (0) inside a previous thickened area (Figs 5 and 6). The last phenomenon occurs in the eastern part of the plate near the free boundaries NB and BC.

The thickening limit can be interpreted in terms of relaxation as mentioned before and the role of the boundary conditions on such a relaxation process is important.

The fixed boundary AD seems to delay such a relaxation mechanism and the thickening limit is not observed in this part of the plate during the deformation; only a slow decrease of the vertical strain rates occurs. On the contrary the free boundary conditions at NB and BC increase the relaxation mechanism and allow the individualization of the distensive areas on the side of the punch where the crust has already been significantly thickened and where the rotational boundary interactions are important. Because of the non-linearity of the problem this decrease is not uniform in the plate. Each material point follows the finite transformation with its own thickening history and its own relaxation properties. This is the reason why the distensive areas are not located in front of the punch but on the side of it following the advective transport.

Influence of the Argand number. Its influence is quite clear from Fig. 6. To increase the Argand number tends to decrease the relaxation time. As the Argand number increases the relaxation mechanism becomes noticeable during the evolution of the deformation. Distensive effects consecutive to the thickening limit of certain areas can be induced locally and a fast decrease of the vertical strain rates is generally observed. For Ar = 700 these distensive areas, which are quite important, are located in already thickened areas, and clearly related to free boundaries NB and BC.

Influence of the plastic effects. The vertical strain becomes more concentrated with strong relaxation phenomena. Distensive effects are less noticeable.

5.2 HETEROGENEOUS LITHOSPHERE

The geometry of the deformation is deeply changed by the presence of an initial stiffer inclusion inside the plate.

The initial geometry of this inclusion can be quite arbitrary, although we choose one that corresponds approximately to the actual shape of the Tarim depression in Asia (Fig. 1).

Results are presented here for a rigidity ratio $R = 2.5$ and two sizes of inclusion (Fig. 3b, c). Figs 10 and 11 show the evolution at $t = 0.6\,t_c$ and $0.84\,t_c$ respectively for two dimensions of heterogeneity and Ar = 700. Finally Fig. 15 illustrates the evolution of the crustal thickness along the retained profile of a 'large inclusion' and different values of the Argand number: Ar = 500, 700, 900.

5.2.1 Second invariant of the strain rate tensor

The main feature is the progressive growth of the two intense shear zones in relation to this inclusion (Figs 10 and 11, GL and G) or Fig. 12 (N1 and N2).

The first one expands along the edge EH of the inclusion and is taken over progressively towards the free boundary AM, on the side of the punch. This shear zone spreads, contorts around the inclusion in the northern boundary, and is related to the displacement-rotation of the inclusion itself under the horizontal pressure of the punch.

The second one expands in front of the inclusion, along the edge EF and reaches its maximum intensity at the end of that edge. This shear controls a strong lateral extrusion of the material in front of the punch towards the free boundaries NB and NC. The extrusion increases during the indentation as the crustal thickening is reaching its relaxation limit and at the end it absorbs most of the convergence process. Associated with this extrusion
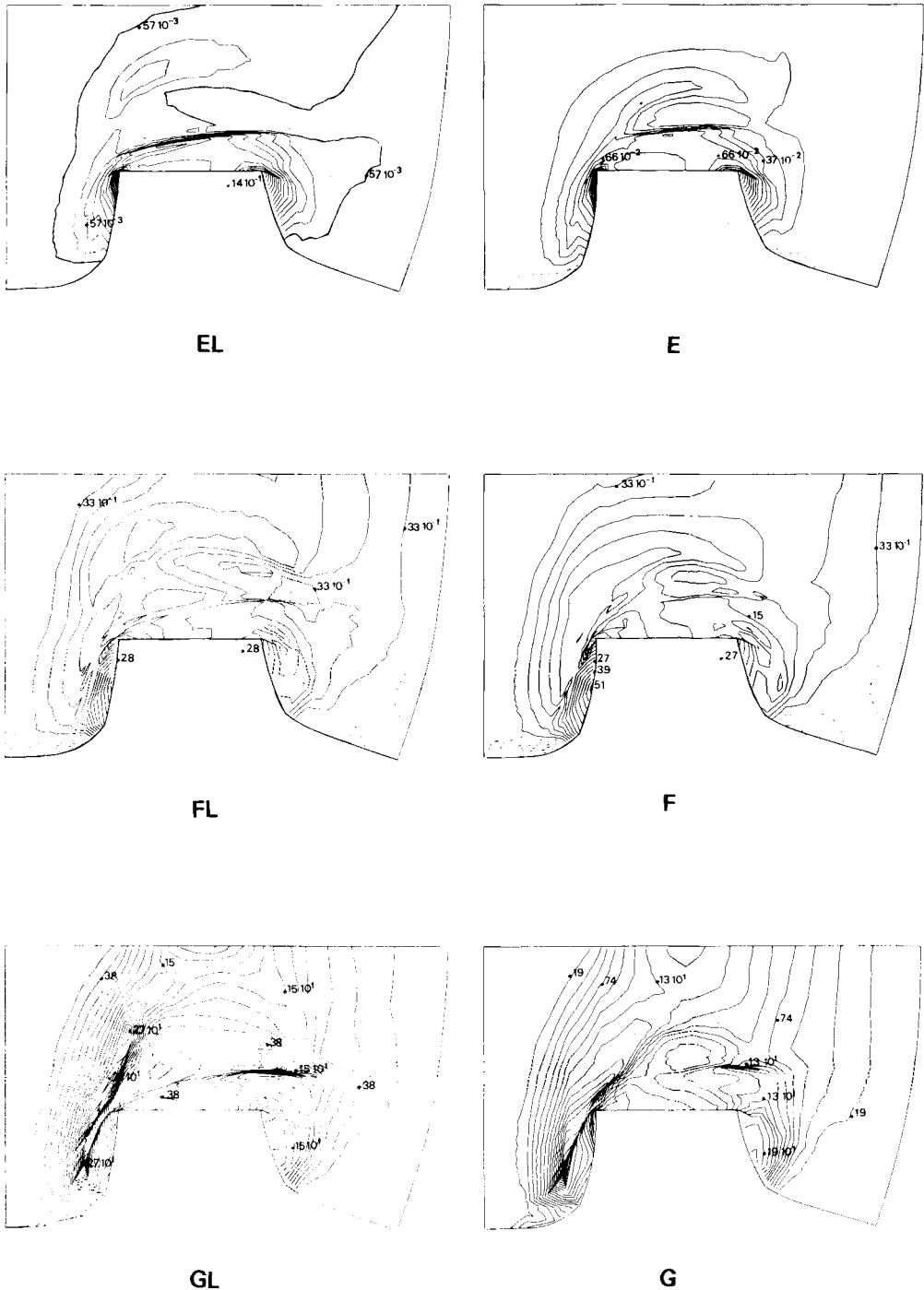
Figure 10. Heterogeneous plate at $t6 = 0.6\,t_C$ with a small inclusion (E, F, G) and a large one (EL, FL, GL), and $R = 2.5$: E and EL: normalized crustal thickness evolution: E: 18 isovalues (-0.27×10^{-2}, 0.19×10^{-1}, 0.11×10^{-2}), EL: 18 isovalues (-0.11×10^{-2}, 0.20×10^{-1}, 0.11×10^{-2}). F and FL: vertical strain rate: F: 18 isovalues (-0.16, 0.50, 0.39×10^{-1}), FL: 19 isovalues (-0.21, 0.52, 0.41×10^{-1}). G and GL: second invariant of the strain rate tensor: G: 18 isovalues (0.18, 3.34, 0.18), GL: 19 isovalues (0.19, 3.6, 0.19).

Figure 11. Heterogeneous plate at $t8 = 0.84\,t_c$ (as Fig. 10): E and EL: normalized crustal thickness evolution, E: 19 isovalues $(-0.27 \times 10^{-2}, 0.20 \times 10^{-1}, 0.11 \times 10^{-2})$, EL: 20 isovalues $(-0.58 \times 10^{-2}, 0.21 \times 10^{-1}, 0.11 \times 10^{-2})$. F and FL: vertical strain rates: F: 19 isovalues $(-0.20, 0.50, 0.39 \times 10^{-1})$, FL: 19 isovalues $(-0.25, 0.48, 0.41 \times 10^{-1})$. G and GL: second invariant of the strain rate tensor: G: 20 isovalues $(0.18, 3.71, 0.18)$, GL: 20 isovalues $(0.19, 3.00, 0.19)$.
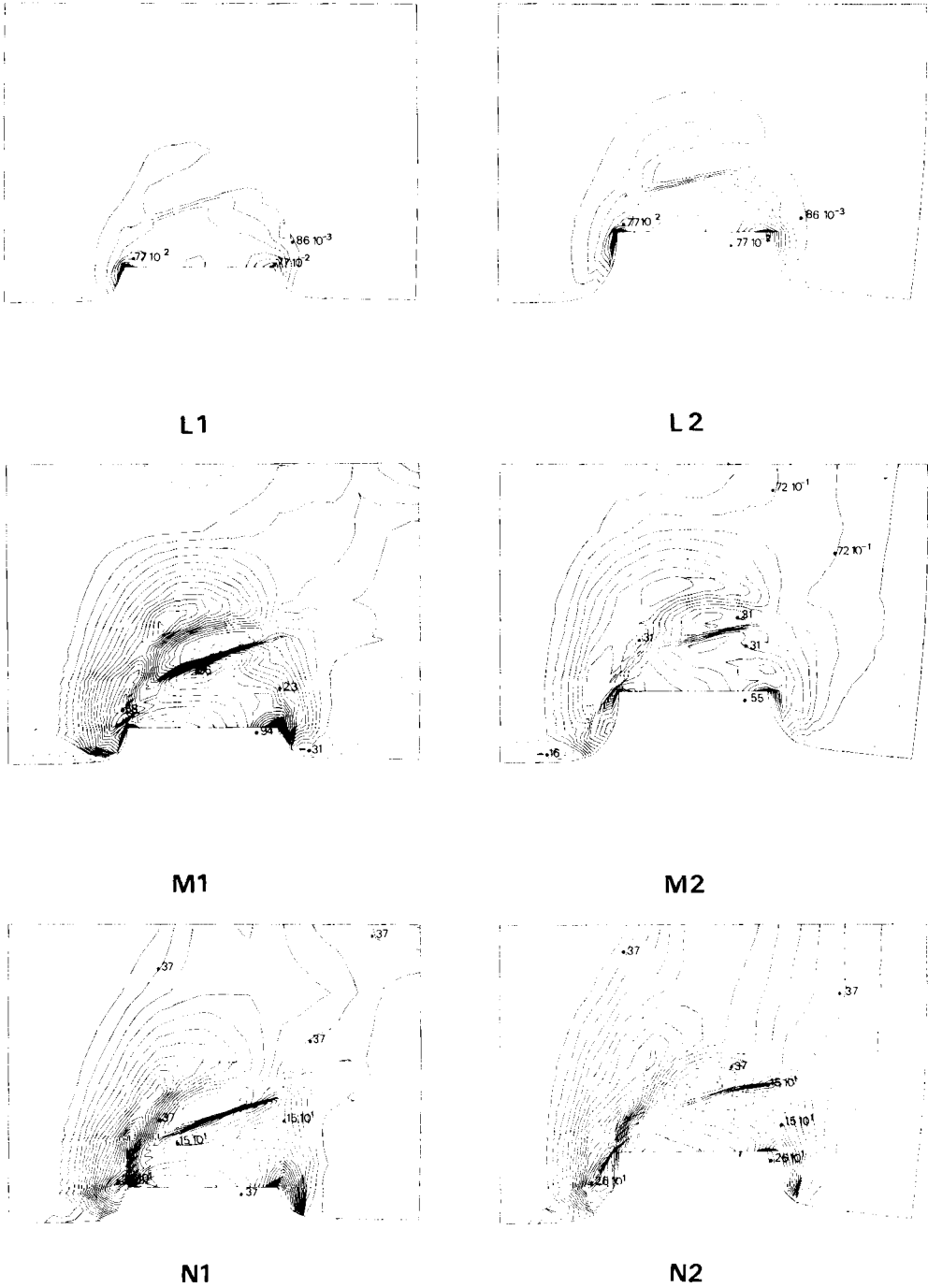
Figure 12. Heterogeneous plate with small inclusion at $t2 = 0.24\,t_c$ (L1, M1, N1), and $t5 = 0.5\,t_c$ (L2, M2, N2), and $R = 2.5$: L1 and L2: normalized crustal thickness evolution: L1: 13 isovalues $(-0.27 \times 10^{-2}, 0.13 \times 10^{-1}, 0.11 \times 10^{-2})$, L2: 17 isovalues $(-0.27 \times 10^{-2}, 0.18 \times 10^{-1}, 0.11 \times 10^{-2})$. M1 and M2: vertical strain rates: M1: 34 isovalues $(-0.12, 1.17, 0.39 \times 10^{-1})$, M2: 22 isovalues $(-0.16, 0.66, 0.39 \times 10^{-1})$. N1 and N2: second invariant of the strain rate tensor: N1: 21 isovalues $(0.18, 3.9, 0.18)$, N2: 18 isovalue $(0.18, 3.34, 0.18)$.

process, a strong clockwise rotation occurs and explains the significant quasi-rigid rotation of the inclusion as well as the progressive bending of the shear zone.

The intensity and extension of these shear zones are clearly controlled by the size of the inclusion (Figs 10 and 11) and by the rigidity ratio R. As this ratio increases (i.e. as the inclusion becomes more and more rigid), the shear increases. This phenomena is discussed in detail for plane strain by Vilotte *et al.* (1984).

These shear zones give in certain parts very high values for the gradients of deformation, which are strongly localized and could be regarded as a continuous approximation (at the limit) of discontinuity effects such as the observed large strike-slip faults.

5.2.2 Crustal thickness

The change of geometry is here quite spectacular and the presence of an inclusion could be described in term of four principal effects:

(a) It increases significantly the crustal thickness in front of the punch (Figs 10 and 11 (EL and E) and Fig. 12 (L1 and L2)), which can now reach more than 100 per cent (Fig. 15).

(b) The inclusion itself does not present any significant thickening during the deformation (Fig. 15), and sometimes even shows some local thinning.

(c) The stiffer inclusion produces crustal thickening in the areas just behind it. Such a propagation further north of the crustal thickening is not only due to the transmission ahead of the horizontal pressure by the rigid core, but also to the rotation of the inclusion which squeezes the material between its northern end and the free-glide boundary DC. This crustal thickening is controlled by the size of the inclusion.
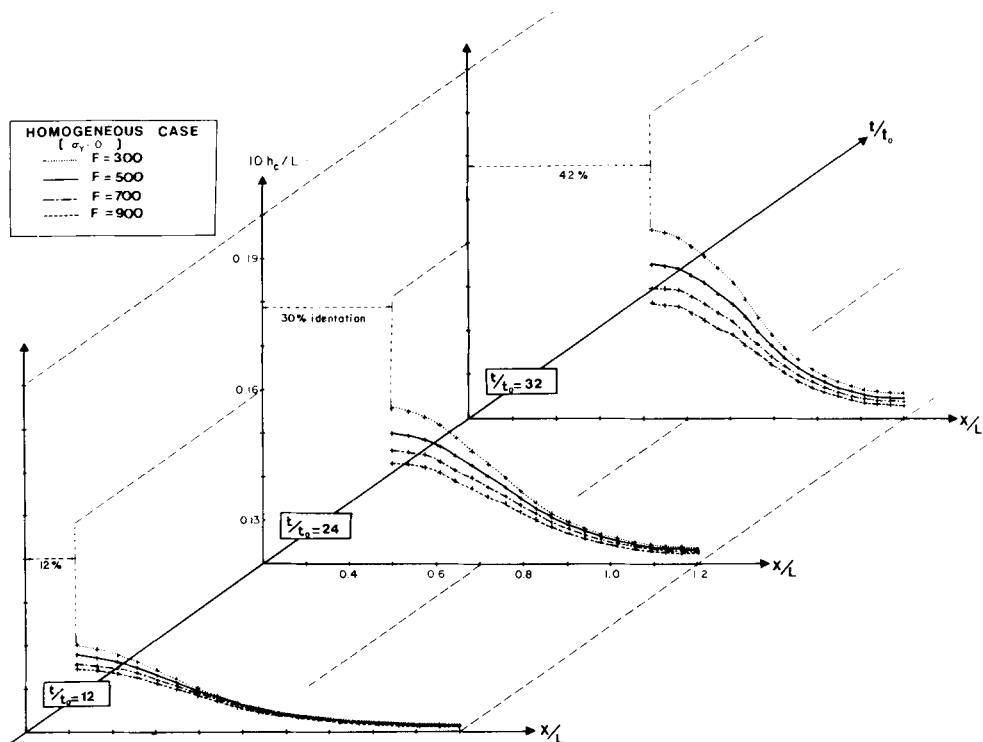

Figure 13. Crustal thickness evolution along a cross-section shown in Fig. 3 in the homogeneous plate for power law creep ($n = 3, K = 0$).
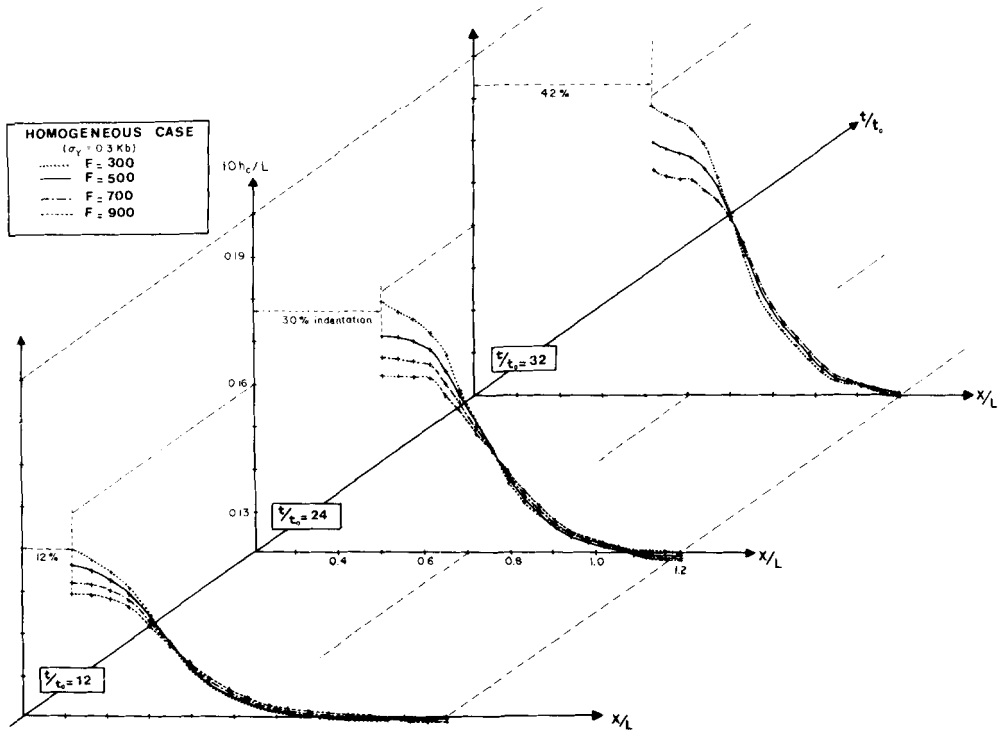
Figure 14. Crustal thickness evolution along a cross-section as in Fig. 13 for plastic flow ($n = 3, K = 2.69$).

(d) Finally on the western side of the inclusion an arc-like structure expands with noticeable crustal thickening and bends during the deformation in relation to the rotation of the inclusion. It also stretches towards the adjacent area of the punch. A thinning zone is localized at the tip of the shear previously described at the eastern end of the edge EH of the inclusion.

Fig. 15 clearly shows that the inclusion does not thicken so that it appears then as a strong depression lined by the southern area with a strong crustal thickening (of the order of 100 per cent) and presenting a slight plateau effect and by the northern area also with a noticeable crustal thickening (of the order of 40–50 per cent) and rounded topography.

Effects of the Argand number. The Argand number has two major effects (Fig. 15):

(a) It flattens the topography in front of the punch which is registered by the presence of the rigid inclusion which prevents spreading phenomena. However due to the small value of the rigidity ratio R, as Ar increases the depression zone is shortened and the transition zone becomes sharper. This flattening effect also tends to intensify the lateral extrusion controlled by the shear zone located along the southern edge of the inclusion.

(b) A more complicated effect on the topography behind the inclusion. As Ar increases this area is shorter and thicker as it is pushed towards the depression zone.

5.2.3 Vertical strain rates

Strong vertical strain rates are localized progressively on the eastern side of the punch and are associated with the rotational effect due to the corner of the punch and the fixed boundary AD. This localization does not exist on the other side of the punch due to the strong lateral extrusion process which dominates the singularity effect.
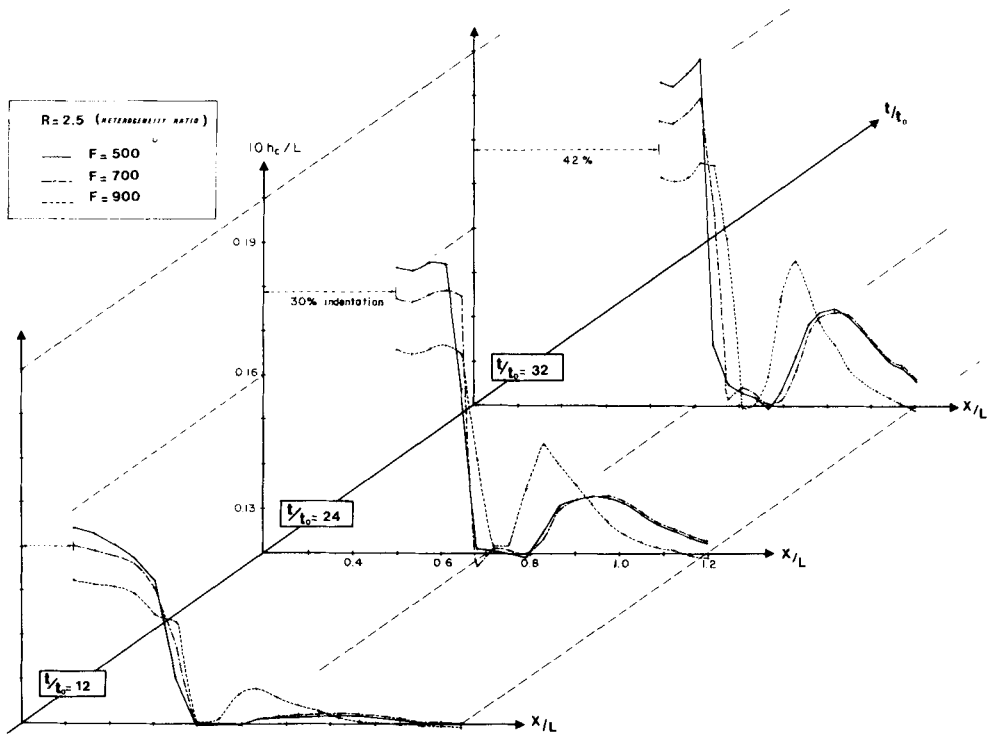
Figure 15. Crustal thickness evolution along a cross-section in the heterogeneous plate (with large inclusion).

Inside the inclusion, the vertical strain rates remain very low and sometimes turn to become negative. A distension zone is localized at the eastern tip of the shear zone along the edge EH.

These local intraplate distensive phenomena are related to the inclusion and are similar to the negative pressure effects which appear in the plane strain case (Vilotte *et al.* 1984).

We simulate the rigid inclusion by a zone of stiffer properties which will tend to a rigid behaviour as *R* increases. The deformation in the inclusion zone tends then to zero and is the only physical variable, while the stress is a conjugate measure which will become meaningless. The velocity field is still continuous but the deformation field is not. The initial geometry and the rigidity contrast of these inclusions remain quite arbitrary. These more rigid blocks are often characterized as colder continental lithosphere and it is important to notice that the lack of significant thickening evolution during the deformation process in these areas makes a reheating phenomenon unlikely to happen unless local heat sources are supposed to lie underneath. Furthermore, even if strong shear heating is likely to happen along the edges of that inclusion, with lateral heat conduction such a process will remain very slow and then limited during the deformation and these rigid zones will remain very stable during that period.

6 Discussions and conclusions

In order to draw geodynamical conclusions from the numerical experiments and to bring out some open questions, we discuss the results with reference to the Indian—Asian collision. However one has to bear in mind that these numerical experiments did not intend to model

that specific geodynamical area, but only to point out some physical processes and the influence of the different parameters.

Assuming, as we did, that an isostatic compensation of Airy's type occurs during the deformation, then the buoyancy force effects are expressed as a relaxation mechanism of the crustal thickening. The time-scale of this process is of an order of magnitude of the characteristic time of the horizontal flow.

The buoyancy forces impose a limit to the crustal thickening. The thickening history before that limit and the limit itself depend on the importance of these buoyancy forces, on the rheological non-linearities and even more on the boundary conditions.

During the deformation, the vertical strain rates decrease and as a result of this flattening effect the crustal thickening spreads over the lithospheric plate. Such a spreading strongly couples the horizontal flow to the vertical evolution and adds to the non-linearity of the problem.

The boundary conditions play a crucial role throughout:

The free boundary conditions on the eastern side of the plate (NB and BC) control a lateral extrusion flow with strong clockwise rotational effects which redistributes large continental masses towards that free boundary. The crustal thickening is not contained on the east side of the plate due to these boundary conditions and under the buoyancy forces a thickening limit is quickly reached, then inducing an important extrusion flow. The relaxation process, which is very fast near the free boundary, may induce local distension inside areas previously thickened. Extrusion flow is attested in the homogeneous case by the growth in front and on the side of the indenter of a strong shear which bends progressively due to a clockwise rotation induced as by the free boundaries.

The West Pacific subduction zone could then play an important role on the evolution of the deformation in Asia, its influence extending way inside the plate and its presence allowing a continuous evolution of the indentation process. On the other hand the combined effects of the free boundary conditions and the buoyancy forces could be in good agreement with local distensive areas inside the Asian plate like the Yunan or the south-east part of Indochina, which would then be related to the lateral extrusion towards the eastern free boundaries.

In all the experiments, crustal thickening is mainly localized in front of the punch with a more or less spread geometry depending on the rheological non-linearities and the buoyancy forces. This thickening is mechanically related to the horizontal compression induced by the punch penetration and can be of the order of 40–70 per cent after 30–40 Myr, depending on the models. Most of this crustal thickening is produced at the early stage of the evolution and after 30–40 Myr the limit has almost been reached. High non-linearities ($5 < n < 10$) lead to important crustal thickening (70–100 per cent) in front of the punch with a plateau geometry but the horizontal deformation then becomes too concentrated in the vicinity of the punch, with important lateral rigid zones. Such features do not seem compatible with the actual observations in Asia. In order to keep realistic horizontal deformation one has to accept for homogeneous lithosphere a crustal thickening in front of the punch never higher than 70 per cent.

These final values of the crustal thickness are of the order or often less than those obtained by different studies in Asia dealing either with the dispersion of group and phase velocities of Rayleigh waves (Bird & Toksoz 1977; Chun & Yoshii 1977; Patton 1980; Chen & Molnar 1981), either with velocity and propagation characteristics of *Pn* and *Sn* waves (Chen & Molnar 1981; Barazangi & Ni 1982), either with N–S seismic sounding reported in Hirn *et al.* (1984a, b) and Hirn & Sapin (1984). Typical results of those studies lead to a thick crustal layer of 50–90 km beneath the Tibet area, north of the Indus suture zone.

Strong crustal thickening concentrations are observed in relation to the geometrical singularities of the indenter.

Important lateral shears, adjacent to the punch, are very similar to what is observed at present in Asia as, for example, the Chaman fault or the Pakistan fold belts in the west side of the Indian indenter, and the Red River fault or the Arakan–Burma arc in the eastern side. These features could then result from a concentration of the deformation due to the edges of the Indian plate and to the strong rotational flow associated with them, clockwise on the eastern side and anticlockwise on the western side. The Indian plate should also be deformed near its edges, but that will not change the general features described above.

Associated with these concentrations of the deformation there is also a strong stress concentration as in plane strain analysis. Such local stress concentrations could be responsible for strong seismic activity in those areas, and could indeed explain the localization of the major seismic events of $M \geqslant 7$, from 1897 to 1976, on both corners of the Indian plate as it appears in the catalogue compiled by Chandra (1978).

The numerical models presented here cannot discriminate between the different geodynamical models proposed for the crustal thickening in front of the collision zone. In particular they cannot take into account models such as those of the low angle underthrust type proposed by several authors (Argand 1924; Powell & Canagham 1973, 1975; Barazangi & Ni 1982). However such models seem physically quite complicated since they would involve either a complete split-up of the Asian crust and mantle, or the complete melting of the Indian crust and then its migration through the Asian mantle implying a recycling of a great volume of material (Chen & Molnar 1981).

Numerical results indicate that in any case a quite noticeable crustal thickening has to be associated with horizontal compression due to collision, and a significant part of the convergence between India and Asia must have been absorbed by compression and must still continue to operate, implying then a crustal thickening in front of the punch. Such thickening is likely to happen whatever the preferred geodynamical model is. Recent palaeomagnetic data in Tibet seem to require such a compressional deformation (Allegre *et al.* 1984). The thickening process associated with that compression could be, of course, more or less complicated. It seems in particular that thickening by simple homogeneous shortening as suggested by Dewey & Burke (1973) is unlikely to happen and that thickening associated with intracontinental thrust and a complicated topography of the Moho is in better agreement with recent results from the Franco–Chinese expedition as reported in Hirn *et al.* (1984a, b), Hirn & Sapin (1984), Mathews & Hirn (1984) and Allegre *et al.* (1984).

One of the major results of this study is indeed the dramatic change in the geometry of the deformation when a stiffer inclusion is initially present inside the lithospheric plate.

The Asian plate cannot in fact be regarded as a simple mechanically homogeneous medium since it results from successive and continuous accretions of continental blocks, the driving mechanism itself being an open question (Anderson 1982), and which looks more like a mosaic of suture bounded blocks originating from the initial breakup of the Gondwana continent (Allegre *et al.* 1984; Klimetz 1983) and which accumulated around the Siberian craton since the Palaeozoic and up to the Indian collision itself. Such a pattern introduced strong heterogeneity in the Asian plate when the Indian collision started. The Tarim area, where no deformation associated with the Indian–Asian collision has been observed and no actual seismicity has been reported, should be an old shield accreted to the Siberian craton during a previous Palaeozoic collision (Tapponnier & Molnar 1981). We used its actual shape as a reference for the initial geometry and position of the stiffer inclusion in our models. These old shields are often considered for many reasons but mainly thermal one as more rigid zones.

One major effect is the growth of two main shear zones, controlled (size and shape) by the inclusion, even if the rigidity ratio remains quite small.

One of these shear zones is located along the southern edge of the inclusion and controls an important lateral extrusion of the material initially in front of the punch towards the adjacent free boundaries NB and BC. This shear progressively bends due to strong clockwise rotational effects attested by the rotation of the inclusion itself. The convergence is then absorbed in front of the punch partly by a significant thickening and partly by a strong lateral extrusion controlled by the shear. The latter mechanism becomes more and more important during the deformation in particular because of the crustal thickening limit imposed by the relaxation, and at the end of the evolution most of the convergence is absorbed by the shear along the southern edge of the inclusion. This shear zone is similar to the Altyn Tagh fault in front of the Tarim where strong left-lateral motion controlled mainly the lateral extrusion of the Tibetan lithosphere. The significant rigid rotation of the block, as observed in the numerical results, could have a palaeomagnetic signature, but unfortunately, to the authors knowledge, no such data are available in the Tarim area. The crucial role played by the Altyn Tagh fault, as suggested by the models, has also been pointed out by Tapponnier *et al.* (1983).

The Tibetan lithosphere has been considered here as homogeneous. Recent results of Hirn *et al.* (1984b) and Allegre *et al.* (1984) suggest a Tibetan crust composed in fact of several heterogeneous blocks such as those of Lhassa, Quantang, and Kunlun accreted along recognized sutures which are further used as subvertical strike-slip faults during the Indian convergence. The Tibetan crust would then be strongly heterogeneous and affected by deep intracontinental thrusts. However such heterogeneous blocks should be characterized by very small rigidity ratios and would simply amplify the lateral extrusion process by inducing new shear zones along their boundaries. The main heterogeneity will still remain the Tarim block with a higher rigidity ratio which, from our understanding, controls the main large-scale features of the extrusion flow.

Another shear zone is located along the western boundary of the inclusion. This shear progressively bends and skirts around the inclusion in its northern part. This shear is related to the rotation-translation of the inclusion under the pushing effect of the penetrating punch and is located in the approximate position of Tien Shan. The zone is, however, quite complicated since it has also been associated with the Palaeozoic accretion of the Tarim (Tapponnier & Molnar 1981).

This stiff inclusion also affects the crustal thickening evolution and two major features can be pointed out:

A distensive area with local thinning is individualized at the tip of the shear zone located along the southern edge of the inclusion. Such an area is very similar to Shansi which could then be related to the Altyn Tagh fault and to the lateral extrusion process as already suggested by Tapponnier *et al.* (1983). The position and features of that area would then be controlled by the Tarim heterogeneity.

The inclusion itself does not present any significant thickening and could even be subjected to an occasional thinning process, and appears then as a depression bounded by two important crustal thickening zones in front of the punch (100 per cent) and behind it (40–50 per cent).

A similar profile to the one used in the numerical modelling has been roughly constructed from the topographic data of Lee (1966), recently published by England & McKenzie (1983). Fig. 16 shows how the pattern of the actual topography is now captured by the numerical results and suggests definitely that the continental plate cannot be considered as homogeneous if one wants to explain the Tarim depression and the Tien Shan area.
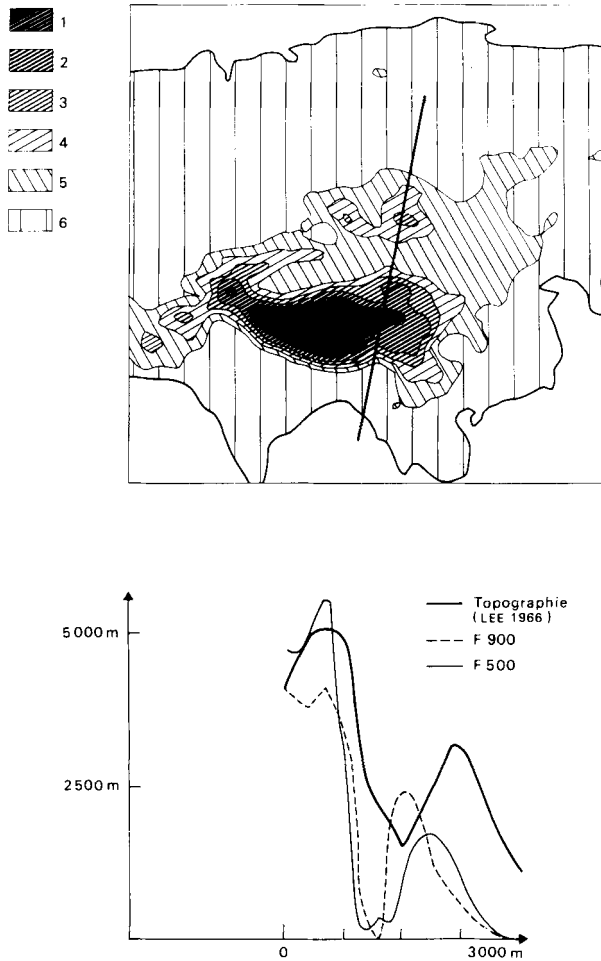
Figure 16. Comparison between a topographic profile derived from the data of Lee (1966) and those derived from numerical experiments at Ar = 700 and 900. (2) $4000 < h < 5000$ m, (3) $3000 < h < 4000$ m, (4) $2000 < h < 3000$ m, (5) $1000 < h < 2000$ m, (6) $h < 1000$ m.

These results, as well as the recent data from Asia, strongly suggest that the continental lithosphere is heterogeneous even at large scales (1 M km). The homogeneous approach has, however, been very useful at the beginning to get a better understanding of the non-linear effects and of the role played by the boundary conditions during a continental collision. We think that it is necessary to estimate the rheological properties of the continental crust and upper mantle and their interactions before proceedings with numerical modelling. Even if the rheological data derived from laboratory experiments (Kirby 1983; Rundle 1983) are of fundamental importance to obtain, special research then has to be done, taking into account the complex thermal and mechanical history of the continental lithosphere in terms of large-scale heterogeneities. Successive accretions lead to a mosaic of heterogeneous blocks of different sizes and different rigidity ratios. In particular the Tibetan heterogeneities seem to be essentially crustal ones (Hirn *et al.* (1984a, b) while there are no data for the Tarim one. However, a strong anomaly of the seismic wave propagation in the upper mantle beneath Tibet suggests azimuthal anisotropy which could be induced by a ductile E–W flow related

to the extrusion process (Hirn *et al.* 1984a, b). The extrusion would then be a major feature affecting the whole lithosphere and should then be controlled by a major heterogeneity such as the Tarim.

At that stage one could speculate and regard the continental crust effectively as a mosaic of blocks of different rigidity ratios, generally small. The horizontal deformation would then be localized along their boundaries in more or less broad shear zones with strong rotational effects thus allowing these blocks to move and rotate with reference to each other. In particular after an initial thickening stage of those blocks, when the relaxation limit is reached, these shear zones (and the boundary conditions) will play a crucial role in allowing the deformation process to continue. The deformation in the upper mantle would be essentially ductile and more homogeneous. The crustal blocks would have then to accommodate this deeper ductile process following the kind of crustal—mantle coupling assumed at the Moho. This deep ductile flow would be controlled by the boundary conditions and could be perturbed by major heterogeneities inducing large-scale anisotropy. Subduction zones will then avoid a locking of the system.

References

Allegre, C. J. *et al.*, 1984. Structure and evolution of the Himalaya-Tibet orogenic belt, *Nature,* **307**, 17–22.

Anderson, D. L., 1982. Hotspots, polar wander, Mesozoic convection and the geoid, *Nature,* **297**, 391–393.

Argand, E., 1924. La tectonique de l'Asie, *Int. geol. Congr. Rep. Sess. 13,* **1**(5), 171–322.

Barazangi, M. & Ni, J., 1982. Velocities and propagation characteristics of *Pn* and *Sn* beneath the Himalayan arc and Tibetan plateau: possible evidence of underthrusting of Indian continental lithosphere beneath Tibet, *Geology,* **10**, 179–185.

Bayer, R. & Lesquer, A., 1980. Les anomalies gravimetriques de la bordure orientale du craton Ouest-Africain: geometrie de la suture Pan Africaine, *Bull. Soc. géol. Fr.,* **6**, 863–876.

Bird, P. & Piper, K., 1980. Plane stress finite element models of tectonic flow in southern California, *Phys. Earth planet. Int.,* **21**, 158–175.

Bird, P. & Toksoz, M. N., 1981. *Development in Precambrian Geology,* Vol. 4, Elsevier, Amsterdam.

Caby, R., Bertrand, J. M. & Black, R., 1981. Pan African ocean closure and continental collision in the Hoggar-Ifforas segment, central Sahara, in *Precambrian Plate Tectonics,* pp. 407–434, ed. Kroner, A.

Chandra, U., 1978. Seismicity, earthquake mechanism and tectonics along the Himalayan mountain range and vicinity, *Phys. Earth planet. Int.,* **16**, 109–131.

Chen, W. P. & Molnar, P., 1981. Constraints on the seismic wave velocity structure beneath the Tibetan plateau and their tectonic implication, *J. geophys. Res.,* **86**, 5937–5962.

Chun, K. Y. & Yoshii, T., 1977. Crustal structure of the Tibetan plateau: a surface wave study by a moving window analysis, *Bull. seism. Soc. Am.,* **67**, 737–750.

Dewey, J. F. & Burke, K. C. A., 1973. Tibetan, Variscan and Pre-Cambrian basement reactivation: products of continental collision, *J. Geol.,* **81**, 683–692.

England, P. & McKenzie, D. P., 1982. A thin viscous sheet model for continental deformation, *Geophys. J. R. astr. Soc.,* **70**, 295–322.

England, P. & McKenzie, D. P., 1983. Correction to a thin viscous sheet model for the continental deformation, *Geophys. J. R. astr. Soc.*, **73**, 523–532.

Goetze, C., 1978. The mechanism of creep in olivine, *Phil. Trans. R. Soc. A*, **288**, 99–119.

Hirn, A., Jobert, G., Wittlinger, G., Zhu Zhong-Xin & Gao En Yuan, 1984a. Main features of the upper lithosphere between the high Himalayas and the Yarlung Zang Po Jiang suture, *Annls. Géophys.*, **2**, 113–119.

Hirn, A., Nercessian, A., Sapin, M., Jobert, G., Xu Zhong Xiu, Gao En Yuan, Lu De Yuan & Teng Ji Wen, 1984b. Lhasa block and bordering sutures a continuation of 500 km Moho traverse through Tibet, *Nature*, **307**, 25–27.

Hirn, A. & Sapin, M., 1984. The Himalayan zone of crustal interaction: Suggestions from explosion seismology, *Annls Géophys.*, **2**, 123–130.

Karner, G. D. & Watts, A. B., 1983. Gravity anomalies and flexure of the lithosphere at mountain ranges, *J. geophys. Res.*, **88**, 10 449–10 477.

Kirby, S. H., 1983. Rheology of the lithosphere, *Rev. Geophys. Space Phys.*, **21**, 1458–1487.

Klimetz, M. P., 1983. Speculations on the Mesozoic plate tectonic evolution of Eastern China, *Tectonics*, **2**, 139–166.

Lee, W. H. K., 1966. Analysis of the Earth's topography, in orbital perturbations from terrestrial gravity data, *Final Rep., contract A.F.(6d)-4171*, Institute of Geophysics and Planetary Physics, University of California, Los Angeles.

Lyon Caen, H. & Molnar, P., 1983. Constraints on the structure of the Himalayas from an analysis of gravity anomalies and a flexural model of the lithosphere, *J. geophys. Res.*, **88**, 8171–8191.

Mandel, J., 1971. *Plasticite et Viscoplasticite*, Cours C.I.S.M., Udine, Springer-Verlag, New York.

Mathews, D. & Hirn, A., 1984. Crustal thickening in Himalayas and Caledonites. *Nature*, **29**, 482–483.

Nguyen, L. D., 1981. Ein Beitrag zur Berechnung instationaerer starr-plastischer Form-aenderungen mit einer Finite-Element Methode, *Fortschr.-Ber. VDI-Z*, **2**, 46.

Patton, H., 1980. Crust and upper mantle structure of the Eurasian continent from the phase velocity and *Q* of surface waves, *Rev. Geophys. Space Phys.*, **18**, 605–625.

Peltzer, G., Tapponnier, P. & Cobbold, P., 1982. Les grands decrochements de l'Est Asiatique, evolution dans le temps et comparaison avec un modele experimental, *C. r. Acad. Sci., Paris*, **294**, 1341–1348.

Powell, C. M. A. & Conaghan, P. J., 1973. Plate tectonics and the Himalayas, *Earth planet. Sci. Lett.*, **20**, 1–12.

Powell, C. M. A. & Conaghan, P. J., 1975. Tectonic models of Tibetan plateau, *Geology*, **3**, 727–731.

Rundle, J. B., 1983. Models of crustal deformation, *Rev. Geophys. Space Phys.*, **21**, 1454–1458.

Silver, E. A., McCaffrey, R. & Smith, R. B., 1983. Collision, rotation and the initiation of subduction in the evolution of Sulawesi, Indonesia, *J. geophys. Res.*, **88**, 9407–9418.

Tapponnier, P., 1977. Evolution du systeme alpin en mediterranee: Poinconnement et ecrasement rigide-plastique, *Bull. Soc. géol. Fr.*, **3**, 437–460.

Tapponnier, P. & Molnar, P., 1976. Slip line field theory and large scale continental tectonics, *Nature*, **264**, 319–324.

Tapponnier, P. & Molnar, P., 1981. A possible dependence of tectonic strength on the age of the crust in Asia, *Earth planet. Sci. Lett.*, **52**, 107–114.

Tapponnier, P., Peltzer, G., Le Dain, A. Y., Armijo, R. & Cobbold, P., 1983. Propagating extrusion tectonics in Asia. New insights from simple experiments with plasticine, *Geology*, **10**, 611–616.

Timoshenko, S. & Woinowski-Krieger, S., 1970. *Theory of Plates and Shells*, McGraw-Hill, New York.

Vilotte, J. P., Daignieres, M. & Madariaga, R., 1982. Numerical modelling of intraplate deformation: simple mechanical models of continental collision, *J. geophys. Res.*, **87**, 10 709–10 728.

Vilotte, J. P., Daignieres, M., Madariaga, R. & Zienkiewicz, O. C., 1984. The role of a heterogeneous inclusion during continental collision, *Phys. Earth planet. Int.*, **36**, 236–259.

Zienkiewicz, O. C., 1984. Flow formulation for numerical solution of forming processes, in *Numerical Analysis of Forming Processes*, pp. 1–43, eds Pittman, J. F. T., Zienkiewicz, O. C., Wood, R. D. & Alexander. J. M., Wiley, London.

Zienkiewicz, O. C., Jain, P. C. & Onate, E., 1978. Flow of solids during forming and extrusion: some aspects of numerical solutions, *Int. J. Solids Struct.*, **14**, 15–38.

Zienkiewicz, O. C. & Heinrich, J. C., 1979. A unified treatment of steady state shallow water and two dimensional Navier Stoke equations, finite element penalty function approach, *Comp. Meth. appl. Mech. Engng*, **17/18**, 673–698.

Appendix

The basic equations of the problem are two-dimensional and all the differential operators used here are defined in R^2.

At every time $t \in [0, T]$ we have to solve:

$$\nabla . (h_1 \, \sigma^e) = 0 \tag{A1}$$

$$\nabla . (h_\beta \, v) = 0 \tag{A2}$$

where β stands for the crust, mantle or lithosphere. Equation (A2) may be rewritten as

$$h_\beta \, \nabla . v = - \frac{D}{Dt} (h_\beta) \tag{A3}$$

where

$$\frac{D}{Dt} = \frac{\partial}{\partial t} . + v . \nabla . \tag{A4}$$

The equivalent averaged stress tensor is given by:

$$\bar{\sigma}^e = - \bar{p}_B^e : 1 + \bar{\sigma}_{PS}^e \tag{A5}$$

where the buoyancy pressure:

$$\bar{p}_B^e = \frac{1}{2} F \frac{\bar{h}_c^2}{h_c} + \frac{1}{2} \rho_2 g \frac{\bar{h}_1^2}{h_1} \tag{A6}$$

and σ_{PS}^e is a pseudo-plane stress tensor

$$\underline{\sigma}_{PS}^e = 2\mu(\nabla . v) + 2\mu(\nabla v + v \nabla). \tag{A7}$$

μ is considered here as a bounded viscosity:

$$\mu_0 \leqslant \mu \leqslant \mu_1 . \tag{A8}$$

The boundary conditions are as follow:

$$v = \tilde{u} \quad \text{on} \quad \partial \Omega' Q(t) \tag{A9}$$

and

$$\sigma_{PS}^e . n = 0 \quad \text{on} \quad \partial \Omega^2 (t) \tag{A10}$$

with also

$$\frac{\partial \bar{p}_B^e}{\partial n} = 0 \quad \text{on} \quad \partial^1 \Omega(t) \tag{A11}$$

and the initial condition

$$h_c(t = 0, x) = h_c \tag{A12}$$

UPDATED LAGRANGIAN

We consider here a Lagrangian evolution of the solution (with the velocity the characteristic direction). At each time $t \in [0, T]$ of the evolution, the reference configuration is updated

to the final one. At any time $t_1 \in [t, \ t + \Delta t]$ of the evolution we have, if (a, b) are the coordinates at t in the reference configuration of a material point x:

$$x(a, b, \tau) = a + \int_t^{t_1} v_x(a, b, \tau) \, d\tau \tag{A13}$$

$$y(a, b, \tau) = b + \int_t^{t_1} v_y(a, b, \tau) \, d\tau \tag{A14}$$

with

$$\frac{\partial x}{\partial \tau} = v_x \quad \frac{\partial y}{\partial \tau} = v_y. \tag{A15}$$

FINITE ELEMENT DISCRETIZATION

Let us introduce the Hilbert space $H'(\Omega)$:

$$(\mathbf{u}, \mathbf{v}) = \int \mathbf{u} \cdot \mathbf{v} \, d\Omega + \sum_{i=1}^{2} \int \frac{\partial u}{\partial x_i} \frac{\partial v}{\partial x_i} \, d\Omega$$

and introduce also the trace operator $\gamma : H_2^1(\Omega) \to H^{1/2}(\Omega)$. The velocity space is 1U defined as:

$$K : \{\mathbf{v} : \mathbf{v} \in H^1(\Omega), \gamma(\mathbf{v}) = \mathbf{u} \text{ on } \partial^1 \Omega(t)\}$$

and the crustal thickness space is simply $Q \in L_2(\Omega)$.

The divergence operator is defined as $\boldsymbol{\nabla}. : H^1(\Omega) \to L_2(\Omega)$ and the gradient operator as: $\boldsymbol{\nabla} : L_2(\Omega) \to H^{-1}(\Omega)$.

The first step of the algorithm can be written as:

find $v^n \in K\ [\Omega\,(t_n)]$, knowing $h^n \in Q\ [\Omega\,(t_n)]$ such that:

$$a(\mathbf{v}^n, \mathbf{w}^n) + (\boldsymbol{\nabla} \cdot \mathbf{v}^n, \boldsymbol{\nabla} \cdot \mathbf{w}^n)_\mu = -F\,(h^n\,\boldsymbol{\nabla}\,h_c^n, \mathbf{w}^n)\ \ \forall \mathbf{w}^n \in K$$

with

$$a(\mathbf{v}, \mathbf{w}) = \int h_1^n\,\bar{\mu}(\mathbf{x}^n)\,\dot{\epsilon}\,(\mathbf{v}^n) : \dot{\epsilon}(\mathbf{w}^n)\,d\Omega$$

$$(\boldsymbol{\nabla} \cdot \mathbf{v}^n, \boldsymbol{\nabla} \cdot \mathbf{w}^n)_\mu = \int h_1\,\bar{\mu}\,(\boldsymbol{\nabla} \cdot \mathbf{v}^n)\,(\boldsymbol{\nabla} \cdot \mathbf{w}^n)\,d\Omega$$

at that stage knowing $\boldsymbol{\nabla}. v^n$ one has to find $h_c^{n+1}\ \in Q\ [\Omega\,(t_{n+1})]$:

$$\frac{1}{\Delta t}\,(q^{n+1}, h_c^{n+1} - h_c^n) + (q^{n+1}, h_c^{n+1/2}\,\boldsymbol{\nabla}. v^n) = 0\ \ \forall q^{n+1}\ \in Q(\Omega_{n+1}).$$

The solution will be sought in finite dimensional subspaces $K^h \subset K$ and $Q^h \subset Q$ whose bases are a set of polynomials with small compact support. We consider here the particular case of a continuous piecewise biquadratic approximation for v and continuous piecewise bilinear for h, defined on a discretization Ω^h of rectangular elements where h is a characteristic mesh parameter. Let p (resp. p') be the number of nodes of the velocity (resp. thickness) discretization. We seek an approximation $v_h(x)$ and $h_h(x)$ of the form:

$$\mathbf{v}_h(\mathbf{x}) = \sum_{i=1}^{p} \mathbf{v}_{hi}\psi_i(\mathbf{x})$$

$$h_{ch}(\mathbf{x}) = \sum_{i=1}^{p} h_{chi}\,\varphi_i(\mathbf{x})$$

11

with

$$\psi_i(x_j) = \begin{bmatrix} 1 & i = j \\ \varphi & i \neq j \end{bmatrix} \quad i, j = 1, \ldots p$$

and the same relations for φ_i.

The discretized version of the algorithm is:

suppose h_{ch}^n known as t^n, find $v_h^n \in K^h[\Omega^h(t_n)]$:

$$a(v_h^n, w_h^n) + (\boldsymbol{\nabla} \cdot v_h^n, \boldsymbol{\nabla} \cdot w_h^n)_\mu = F(\boldsymbol{\nabla} h_{ch}^n, w_h^n) \quad \forall \, [w^n \in K^h(\Omega^h(t_{n+1})]$$

update the mesh and the reference configuration;

find $h_{ch}^{n+1} \in Q^h[\Omega^h(t_{n+1})]$, knowing $\boldsymbol{\nabla} \cdot v_h$:

$$\frac{1}{\Delta t} (q_h, h_{ch}^{n+1} - h_{ch}^n) + (q_h, h_{ch}^{n+1/2} \boldsymbol{\nabla} \cdot v_h^n) = \mathbf{0}.$$

The first non-linear set of equations is solved by a Newton–Raphson method and five to seven iterations are needed, while the second set is solved interatively using a lump mass matrix in order to reduce the core storage requirement and also for large systems the number of arithmetic operations, two or three iterations are generally needed. All the runs were performed on a CDC 7600 machine.